Intracellular ion accumulation in the genesis of complex action potential dynamics under cardiac diseases

Xinyu Wang,

Julian Landaw,

Zhilin Qu[*]

Department of Medicine (Cardiology), David Geffen School of Medicine, University of California, Los Angeles, California 90095, USA

Abstract

Intracellular ions, including sodium (Na^+), calcium (Ca^{2+}), and potassium (K^+), etc., accumulate slowly after a change of the state of the heart, such as a change of the heart rate. The goal of this study is to understand the roles of slow ion accumulation in the genesis of cardiac memory and complex action-potential duration (APD) dynamics that can lead to lethal cardiac arrhythmias. We carry out numerical simulations of a detailed action potential model of ventricular myocytes under normal and diseased conditions, which exhibit memory effects and complex APD dynamics. We develop a low-dimensional iterated map (IM) model to describe the dynamics of Na^+, Ca^{2+} and APD and use it to uncover the underlying dynamical mechanisms. The development of the IM model is informed by simulation results under the normal condition. We then use the IM model to perform linear stability analyses and computer simulations to investigate the bifurcations and complex APD dynamics, which depend on the feedback loops between APD and intracellular Ca^{2+} and Na^+ concentrations and the steepness of the APD response to the ion concentrations. When the feedback between APD and Ca^{2+} concentration is positive, a Hopf bifurcation leading to periodic oscillatory behavior occurs as the steepness of the APD response to the ion concentrations increases. The negative feedback loop between APD and Na^+ concentration is required for the Hopf bifurcation. When the feedback between APD and Ca^{2+} concentration is negative, period-doubling bifurcations leading to high periodicity and chaos occurs. In this case, Na^+ accumulation plays little role in the dynamics. Finally, we carry out simulations of the detailed action potential model under two diseased conditions, which exhibit steep APD responses to ion concentrations. Under both conditions, Hopf bifurcations leading to slow oscillations or period-doubling bifurcations leading to high periodicity and chaotic APD dynamics occur, depending on the strength of the ion pump—$Na^+ - Ca^{2+}$ exchanger. Using functions reconstructed from the simulation data, the IM model accurately captures the bifurcations and dynamics under the two diseased conditions. In conclusion, besides using computer simulations of a detailed high-dimensional action-potential model to investigate the effects of slow ion accumulation and short-term memory on bifurcations and genesis of complex APD dynamics in cardiac myocytes under diseased conditions, this study also provides a low-

[*] zqu@mednet.ucla.edu .

dimensional mathematical tool, i.e., the IM model, to allow stability analyses for uncovering the underlying mechanisms.

I. INTRODUCTION

The heart rhythms exhibit rich nonlinear dynamics, which have been widely investigated [1–5]. These dynamics may be precursors or causes of lethal cardiac arrhythmias [6,7]. The normal heart rate is around 60 to 100 beats per minute, corresponding to periods of 0.6 to 1 s. If everything recovers fast enough, changes occurring within a heartbeat do not affect the behavior of the next heartbeat, and thus there is no memory effect. However, many processes exhibit much longer timescales, and a temporal change may take many beats or a much longer time to recover. This long recovery process is called cardiac memory. Memory in the heart may last seconds to minutes, which is called short-term memory, or hours to days, which is called long-term memory [8]. A direct effect of memory is that it affects the rate dependence [9] of the action-potential (AP) properties. For example, as shown in Fig. 1(a), a sudden change in heart rate takes more than 1 min for the AP duration (APD) to reach a new steady state in the human heart [10]. It has been widely shown that short-term memory affects cellular AP and excitable wave dynamics [11–20].

There are two major sources of short-term memory. The first one is slow ion channel recovery which has a timescale of several hundred milliseconds to seconds. For example, the recovery time constant of the potassium $\left(K^+\right)$ channel can be a couple of seconds [21]. It has also been shown that there is a very slow component of the recovery of the L-type calcium $\left(Ca^{2+}\right)$ current ($I_{Ca,L}$) [22–24]. The second source is intracellular ion accumulation which has a timescale of several seconds to minutes. In cardiac myocytes, as well as in many other types of excitable cells [25], ion concentration gradients across the cell membrane are required for a negative (polarized) resting potential and excitability. The major ions [Fig. 1(b)] are the sodium ion $\left(Na^+\right)$, potassium ion $\left(K^+\right)$, and calcium ion $\left(Ca^{2+}\right)$. Their concentrations in the extracellular space (denoted as $\left[Na^+\right]_o$, $\left[K^+\right]_o$, and $\left[Ca^{2+}\right]_o$) are roughly $\left[Na^+\right]_o = 140$ mM, $\left[K^+\right]_o = 4$ mM, and $\left[Ca^{2+}\right]_o = 1.5$ mM, and in the intracellular space (denoted as $\left[Na^+\right]_i$, $\left[K^+\right]_i$, and $\left[Ca^{2+}\right]_i$) are roughly $\left[Na^+\right]_i = 10$ mM, $\left[K^+\right]_i = 150$ mM, and $\left[Ca^{2+}\right]_i = 0.1$ μM. The ion gradients between the intracellular space and extracellular space are primarily maintained by ion pumps, namely, the $Na^+ – K^+$ ATPase (NKA) and the $Na^+ – Ca^{2+}$ exchange (NCX). During an AP, Na^+ and Ca^{2+} enter the cell via the voltage-gated Na^+ channels and Ca^{2+} channels, respectively, and K^+ exits the cell via the voltage-gated K^+ channels. These ions are extruded out or brought into the cell by the ion pumps, forming an inside-outside cycle of the ions. In addition to the inside-outside cycle, Ca^{2+} exhibits an intracellular cycling loop [Fig. 1(b)]. Ca^{2+} is mainly stored in the intracellular organelle called the sarcoplasmic reticulum (SR), and Ca^{2+} in the SR is released into the cytosolic space via the Ca^{2+} release channels on the SR membrane called ryanodine receptors (RyRs). Since the intracellular ion concentrations affect ionic currents

via ion channels and pumps, and the ionic currents affect the ion concentrations, feedback loops form between voltage and the ion concentrations. Moreover, the recovery of different types of ion channels and the accumulation speed of different types of intracellular ions exhibit different timescales. The feedback loops and the multiple timescales can result in very complex dynamics, such as bursting behaviors seen in many biological cells, including neurons [26–28], pancreatic β cells [26], and cardiac cells [29–31].

In recent studies [19,20,32,33], complex AP dynamics caused by ion accumulation and the feedback loops between voltage and ion concentrations in periodically paced ventricular myocytes have been investigated. We have developed low-dimensional iterated map (IM) models that account for the different timescales and feedback loops [18–20]. The IM models can accurately capture the complex dynamics of the high-dimensional AP models and reveal the underlying mechanisms and bifurcations for complex APD dynamics, including bistability, Hopf bifurcations to oscillation, and period-doubling routes to chaos. In this study, we extend our previous work [20] to include a detailed description of the development of the IM model and its validation against simulations of the detailed AP model. We simulate the AP model under two diseased conditions to demonstrate the bifurcations and complex APD dynamics. Specifically:

1. We carry out simulations using a detailed AP model [34] under normal condition to inform the development of the IM model, i.e., the formulation of the IM equations and functions. We use the IM model to simulate the memory effects observed in the AP model under the normal condition as a first validation of the IM model. The results are presented in Sec. III A.

2. We perform linear stability analyses and carry out computer simulations of the IM model to reveal the dynamical mechanisms and the roles of ion accumulation and the feedback loops in the genesis of complex APD dynamics. The stability analyses and simulations show that besides the requirement of a steep response of APD to the change of the ion concentrations, the feedback loops between APD and $\left[\mathrm{Ca}^{2+}\right]_i$ and $\left[\mathrm{Na}^+\right]_i$ play important roles. When the feedback between APD and $\left[\mathrm{Ca}^{2+}\right]_i$ is positive, a Hopf bifurcation leading to periodic oscillatory behavior occurs. The negative feedback loop between APD and $\left[\mathrm{Na}^+\right]_i$ is required for the Hopf bifurcation. When the feedback between APD and $\left[\mathrm{Ca}^{2+}\right]_i$ is negative, a period-doubling bifurcation leading to high periodicity and chaos occurs. In this case, Na^+ accumulation plays little role in the bifurcations and dynamics. The results are presented in Sec. III B.

3. To validate the theoretical predictions of the IM model, we investigate the roles of ion accumulation in the genesis of complex APD dynamics using the detailed AP models under two diseased conditions that exhibit high risk of arrhythmias and sudden cardiac death. The first condition is relevant to long-QT syndrome (LQTS) [35,36] and heart failure [37], in which APD is lengthened due to increase of inward currents (mainly Na^+ and Ca^{2+} currents) or decrease of outward currents (mainly K^+ currents). A well-known phenomenon

under LQTS is a behavior called early afterdepolarizations (EADs) [Fig. 2(a)], which are abnormal depolarizations during the AP plateau. Theoretical studies have shown that EADs are also a result of bifurcations caused by dynamical instabilities [38–39]. Alterations of ionic current properties in LQTS or heart failure promote EADs [40–42] and EAD-related complex nonlinear dynamics, including alternans and chaos [7,38,43–45], which are related to lethal ventricular arrhythmias [7,46]. The second condition is relevant to a disease called Brugada syndrome [47,48]. A potential mechanism of arrhythmias for Brugada syndrome is called phase-2 reentry, which is known to be caused by an AP phenomenon called spike-and-dome morphology [Fig. 2(b)] [49–55]. It has been shown that complex APD dynamics, including alternans and chaos, can occur due to the spike-and-dome AP morphology [19,54,56,57]. Under both diseased conditions, an all-or-none behavior (to or not to exhibit an EAD or a spike-and-dome morphology) gives rise to steep APD responses to the change of ion concentrations, which are necessary for the complex APD dynamics as predicted in the IM model. Under both conditions, we can change the NCX activity to change the feedback properties between APD and $\left[Ca^{2+}\right]_i$ to result in different bifurcations leading to either oscillatory dynamics or high periodicity and chaos. The results are presented in Secs. III C and III D.

4. To quantitatively capture the bifurcations and complex APD dynamics, we use the simulation data of the AP model under the two diseased conditions to reconstruct IM functions and then carry out simulations of the IM model. Under both conditions, the IM model can accurately capture the bifurcations and APD dynamics of the AP model. The results are presented in Secs. III C and III D.

The general conclusions from this study are that ion accumulation can play important roles in the genesis of arrhythmogenic complex APD dynamics in cardiac diseases. The bifurcations and complex dynamics, as well as the corresponding physiological and dynamical mechanisms, can be accurately revealed using low-dimensional IM approaches.

II. COMPUTATIONAL MODELS AND METHODS

A. The AP model

We carry out single-cell simulations using a human ventricular AP model developed by ten Tusscher *et al.* in 2004 [34], and we abbreviate it as the TP04 model. The AP model contains multiple differential equations with complex functions to describe the dynamics of voltage (V), intracellular ion concentrations, as well as multiple gating variables regulating ionic currents. The differential equation for V is

$$C_m \frac{dV}{dt} = -I_{\text{ion}} + I_{\text{sti}},$$

(1)

where $C_m = 1\ \mu\ \text{F/cm}^2$ is the membrane capacitance and I_{sti} is the stimulus current density, which is a 2-ms square pulse of amplitude $26\ \mu\ \text{A/cm}^2$. I_{ion} is the total ionic current density, which is composed of the following individual ionic currents, i.e.:

$$I_{\text{ion}} = I_{\text{Na}} + I_{\text{K1}} + I_{\text{to}} + I_{\text{Kr}} + I_{\text{Ks}} + I_{\text{Ca,L}} + I_{\text{NCX}} + I_{\text{NaK}} + I_{\text{pCa}} + I_{\text{pK}} + I_{\text{bCa}} + I_{\text{bNa}}.$$

(2)

The ionic currents are functions of V, gating variables, and ion concentrations. The gating variables are also described by differential equations in the form of the Hodgkin-Huxley formulation [58]. The ion concentrations are determined by the balance of the corresponding ionic currents. The differential equation for $\left[\text{Na}^+\right]_i$ is

$$\frac{d\left[\text{Na}^+\right]_i}{dt} = -\frac{I_{\text{Na}} + I_{\text{bNa}} + 3I_{\text{NaK}} + 3I_{\text{NCX}}}{V_c F},$$

(3)

where V_c is the cell volume and F is the Faraday constant. The differential equation for $\left[\text{K}^+\right]_i$ is

$$\frac{d\left[\text{K}^+\right]_i}{dt} = -\frac{I_{\text{K1}} + I_{\text{to}} + I_{\text{Kr}} + I_{\text{Ks}} - 2I_{\text{NaK}} + I_{\text{pK}} + I_{\text{sti}}}{V_c F}$$

(4)

For $\left[\text{Ca}^{2+}\right]_i$, the differential equation for the total $\left[\text{Ca}^{2+}\right]_i \left(\left[\text{Ca}^{2+}\right]_{\text{itotal}}\right)$ is

$$\frac{d\left[\text{Ca}^{2+}\right]_{\text{itotal}}}{dt} = -\frac{I_{\text{Ca,L}} + I_{\text{pCa}} + I_{\text{bCa}} - 2I_{\text{NCX}}}{2V_c F} + I_{\text{leak}} - I_{\text{up}} + I_{\text{rel}},$$

(5)

where $\left[\text{Ca}^{2+}\right]_{\text{itotal}}$ includes both free cytosolic Ca^{2+} concentration $\left(\left[\text{Ca}^{2+}\right]_i\right)$ and buffered cytosolic Ca^{2+} concentration $\left(\left[\text{Ca}^{2+}\right]_{\text{ibufc}}\right)$, i.e., $\left[\text{Ca}^{2+}\right]_i = \left[\text{Ca}^{2+}\right]_{\text{itotal}} - \left[\text{Ca}^{2+}\right]_{\text{ibufc}}$, and $\left[\text{Ca}^{2+}\right]_{\text{ibufc}} = \frac{\left[\text{Ca}^{2+}\right]_i \times \text{bufc}}{\left[\text{Ca}^{2+}\right]_i + \text{K}_{\text{bufc}}}$. Similarly, for SR Ca^{2+} concentration, the differential equation for the total $\left[\text{Ca}^{2+}\right]_{SR} \left(\left[\text{Ca}^{2+}\right]_{\text{SRtotal}}\right)$ is

$$\frac{d\left[\text{Ca}^{2+}\right]_{\text{SRtotal}}}{dt} = \frac{V_c}{V_{SR}}\left(-I_{\text{leak}} + I_{\text{up}} - I_{\text{rel}}\right).$$

(6)

One can then calculate the free SR Ca^{2+} concentration $\left(\left[Ca^{2+}\right]_{SR}\right)$ as the total SR Ca^{2+} concentration minus buffered SR Ca^{2+} concentration, i.e.,

$$\left[Ca^{2+}\right]_{SR} = \left[Ca^{2+}\right]_{\text{SRtotal}} - \left[Ca^{2+}\right]_{\text{SRbufc}}.$$

For definitions of variables and parameters, detailed mathematical formulations of the ionic currents, as well as the differential equations of the other variables, one is refered to the original article by ten Tusscher *et al.* [34]. For numerical simulations of the differential equations, an adaptive time step of $\Delta t = 0.005$ to 0.05 ms is used.

B. Model modifications for the EAD case

To generate EADs, we make the following modifications to the TP04 model [20]: I_{to} and I_{Kr} are removed, the maximum conductance of I_{Ks} is reduced, i.e., $G_{Ks} = 0.125$ mS/cm^2, and $I_{Ca,L}$ is substituted by the formulation by Huang *et al.* [59]. We vary the maximum NCX activity (k_{NCX}) to result in different AP dynamics. Figure 2(a) shows an AP without EADs at a lower $I_{Ca,L}$ conductance and an AP with an EAD at a highr $I_{Ca,L}$ conductance. EAD is an all-or-none behavior which causes discontinuous changes of APD during the transiotions between an AP without EAD and an AP with EAD. Except for Fig. 2(a), $G_{Ca,L} = 0.00014$ cm^3/ μ F/s is used in all simualtions for the EAD case.

C. Model modifications for the case of spike-and-dome AP morphology

For the case of spike-and-dome AP morphology, we substitute I_{to} in the original TP04 model with $I_{to,f}$ by Mahajan *et al.* [60]. Other parameter changes of the original TP04 model include decreasing $G_{Ca,L}$, i.e., $G_{Ca,L} \rightarrow 0.89G_{Ca,L}$, and increasing G_{Kr}, i.e., $G_{Kr} \rightarrow 1.45G_{Kr}$. Spike-and-dome AP morphology is an AP property induced by I_{to}: spike-and-dome AP occurs at intermediate I_{to} and spike AP occurs when I_{to} is large [Fig. 2(b)]. Spike-and-dome AP morphology is also an all-or-one behavior which causes discontinuous changes of APD during the transitions between a spike AP and a spike-and-dome AP. Except for Fig. 2(b), $G_{to} = 0.19$ mS/cm^2 is used in all simulations for the spike-and-dome case.

D. Definitions of the variables, parameters, and units for the IM model

In the IM model, we use APD(a_n), diastolic concentrations of Ca^{2+} (c_n) and Na^+(s_n) as variables [see Fig. 2(c)]. APD is defined as the time duration in which $V > -75\text{mV}$. c_n and s_n are the corresponding concentrations at the time right before each beat. In the IM model and the relevant functions, the units of T and a_n are milliseconds (ms), and the units of c_n and s_n are millimolars (mM). For Ca^{2+} concentration in the SR (c_{SR}), the unit is also mM. The values of the parameters in the IM model are chosen according to this set of units and the units of these parameters are not explicitly listed in this paper.

E. Plotting the simulation data

For ion concentrations, the unit mM is used, but for labeling purpose, micromolar (μM) is used for c_n in all plots. For the bifurcation diagrams in this paper, we drop up to 1000 beats

to get rid of the transient process and then plot the recordings from the following 500 to 2000 beats for each T or k_{NCX}.

III. RESULTS

A. Memory effects due to intracellular ion accumulation

To show the memory effects of ion accumulation on APD, we use the same pacing protocol as in the experiments shown in Fig. 1(a). We first pace the cell at $T = 1$ s for 1000 s (or 1000 beats) for the cell to reach its steady state, and then suddenly switch the pacing period to = 0.5 s. After 2000 beats, we switch it back to = 1 s. Figure 3(a) shows a_n, c_n, s_n, and p_n (diastolic $[K^+]_i$ right before each beat) versus n. After switching T from 1 to 0.5 s, it takes more than 2000 beats to reach the steady state, and a_n changes from 270 to 230 ms. Note that the time taken to reach the steady state is much longer than that from the human heart shown in Fig. 1(a). To distinguish the contributions of intracellular Ca^{2+}, Na^+, and K^+ accumulation, we clamp $[K^+]_i$ and $[Na^+]_i$ at constants separately. Clamping $[K^+]_i$ at a constant exhibits only very small effects on APD, $[Na^+]_i$, and $[Ca^{2+}]_i$ [Fig. 3(b)]. However, clamping $[Na^+]_i$ at a constant exhibits large effects on APD, $[K^+]_i$, and $[Ca^{2+}]_i$ [Fig. 3(c)]. After the sudden switch of T, APD only exhibits a 5-ms change, from 263 to 258 ms, much smaller than that in the free-running case. $[Ca^{2+}]_i$ changes from 0.072 to 0.12 μ M, which is also smaller. Note that during the 2000 beats faster pacing time window (from $n = 1000$ to $n = 3000$), $[K^+]_i$ changes from 140 to 125 mM, but APD only changes less than 1 ms and a very small change occurs in $[Ca^{2+}]_i$, indicating again that $[K^+]_i$ only exhibits very small effects on APD and $[Ca^{2+}]_i$. Therefore, in this study, we do not include $[K^+]_i$ in the IM model and will clamp $[K^+]_i$ in certain simulations of the AP model as clarified later.

B. Development of the IM model

As shown in previous studies [18–20,32,33], ion accumulation can induce complex APD dynamics. In our recent study [20], we developed an IM model incorporating the ion accumulation to describe the APD dynamics. Here, we describe in detail the process of developing the IM model [see Fig. 2(c) for the definition of the variables used in the IM model]. Since $[K^+]_i$ exhibits little effects on APD dynamics (Fig. 3), we ignore its contribution in the IM model.

1. *Formulating the IM equations for* c_n *and* s_n—We first seek to formulate the IM equations for c_n and s_n. Based on simulation data of the AP model [Figs. 4(b) and 4(c)], for fixed T and APD, s_n decays exponentially and c_n decays biexponentially. If s_n is also fixed ($[Na^+]_i$ clamped), c_n then decays exponentially. Based on this observation, we describe c_n and s_n by the following IM equations:

$$c_{n+1} = c_n - \beta_c(c_n - \bar{c}),$$

(7)

$$s_{n+1} = s_n - \beta_s(s_n - \bar{s}),$$

(8)

where $\bar{c}$ and $\bar{s}$ are the steady-state concentrations, and β_c and β_s are two parameters determining how fast c_n and s_n approach their steady states. These two parameters describe the accumulation rates of the two ions. One can rewrite Eqs. (7) and (8) as

$$c_{n+1} - \bar{c} = (1 - \beta_c)(c_n - \bar{c}),$$

(9)

$$s_{n+1} - \bar{s} = (1 - \beta_s)(s_n - \bar{s}).$$

(10)

If $\bar{c}$ and $\bar{s}$ are constant, then the solution of Eq. (9) or Eq. (10) takes the following form: $y_n - \bar{y} = \left(1 - \beta\right)^n (y_0 - \bar{y}) = e^{n\ln(1 - \beta)}(y_0 - \bar{y})$. When $\beta_c = 1$ or $\beta_s = 1$, c_n or s_n instantaneously reaches its steady state, $\bar{c}$ or $\bar{s}$. When $\beta_c = 0$ or $\beta_s = 0$, c_n or s_n will never reach its steady state, which corresponds to the case of holding the concentration constant or being clamped. Therefore, the values of β_c and β_s are between 0 and 1. One can calculate β using data from simulations of the AP model under voltage-clamp conditions as in Fig. 4(a). For instance, using the data and the fitting functions ($c_n = 0.000\,094 - 0.000\,028e^{-n/8.1}$ and $s_n = 13.26 - 1.71e^{-n/124.2}$) shown in Figs. 4(b) and 4(c), one obtains β_c and β_s as follows: $\ln(1 - \beta_c) = -1/8.1$, giving rise to $\beta_c = 0.116$, and $\ln(1 - \beta_s) = -1/124.2$, giving rise to $\beta_s = 0.008$. In the computer simulations of the IM model, we set β_c and β_s close to these values. Since the accumulation speed of $\left[Na^+\right]_i$ is much slower than that of $\left[Ca^{2+}\right]_i$, β_s is much smaller than β_c, i.e.,

$$0 < \beta_s \ll \beta_c < 1.$$

(11)

2. Determining the dependence of $\bar{c}$ and $\bar{s}$ on a_n and T—When T and a_n are fixed in the voltage-clamp protocol, $\bar{c}$ and $\bar{s}$ are constants. However, their values are different with different T and a_n. In other words, $\bar{c}$ and $\bar{s}$ are functions of T and a_n. Moreover, $\bar{c}$ also depends on $\left[Na^+\right]_i$, which is mainly determined by the NCX activity. Therefore, we assume that $\bar{c}$ is a function of T, a_n, and s_n, i.e.,

$$\bar{c} = u(T, a_n, s_n).$$

(12)

Theoretically, $\bar{s}$ may also depend on $\left[Ca^{2+}\right]_i$; however, we ignore this dependence and assume that $\bar{s}$ is a function of T and a_n, i.e.,

$$\bar{s} = w(T, a_n).$$

(13)

There are two reasons for this assumption. First, due to intracellular Ca^{2+} cycling, we cannot clamp $\left[Ca^{2+}\right]_i$ at a constant to determine the dependence of $\bar{s}$ on $\left[Ca^{2+}\right]_i$. Second, $\left[Ca^{2+}\right]_i$ equilibrates much faster than $\left[Na^+\right]_i (\beta_s \ll \beta_c)$; the beat-to-beat influence of $\left[Ca^{2+}\right]_i$ on $\left[Na^+\right]_i$ is small, i.e., a large change in $\left[Ca^{2+}\right]_i$ may only cause a very small change to $\left[Na^+\right]_i$ due to very slow response. For example, in Fig. 4(b), in the presence of varying c_n, s_n still decays exponentially.

To reveal the dependence of $\bar{c}$ and $\bar{s}$ on T, a_n, and s_n, we use the voltage-clamp protocol shown in Fig. 4(a) in which we can either fix or vary T and a_n (as parameters) to observe the responses of $\left[Ca^{2+}\right]_i$ and $\left[Na^+\right]_i$. We can also clamp $\left[Na^+\right]_i$ to observe the response of $\left[Ca^{2+}\right]_i$ alone.

a.   Dependence of $\bar{c}$ on s_n: To determine this dependence, besides fixing T and a_n, we also clamp $\left[Na^+\right]_i$ at different levels to obtain $\bar{c}$. As shown in Fig. 4(d), $\bar{c}$ increases almost linearly with the clamped $\left[Na^+\right]_i$. Similar linear relationships are obtained under the EAD and the spike-and-dome conditions. Note that the steady-state SR Ca^{2+} concentration ($\bar{c}_{SR}$) also increases linearly with the clamped $\left[Na^+\right]_i$, indicating that $\bar{c}$ is linearly proportional to $\bar{c}_{SR}$. Since $\left[Ca^{2+}\right]_i$ accumulates much faster than $\left[Na^+\right]_i$ does, $\bar{c}$ can quickly adjust to the $\left[Na^+\right]_i$ change, and thus we assume the following $\bar{c}$ formulism: $\bar{c} = u(T, a_n) + \delta(s_n - \Delta)$.

b.   Dependence of $\bar{c}$ and $\bar{s}$ on T: Here we use the voltage-clamp protocol with a fixed a_n. Figure 5 shows the simulation results for the three cases: The original TP04 model [Fig. 5(a)], the EAD case [Fig. 5(b)], and the spike-and-dome case [Fig. 5(c)]. Since we fix $a_n = 300$ ms, we scan T starting at 320 ms to cover the short diastolic interval ($d_n = T - a_n$) range. The simulation data indicate that for large T, both $\bar{c}$ and $\bar{s}$ exhibit inverse relations with T in the form $\frac{A}{T + T_0} + B$. For short diastolic intervals, one observes $\left(1 - e^{-(T - a_n)/\tau}\right)$. We give the specific functions fitted from the simulation data for each case in the Fig. 5 caption, which are in the following form: $\dfrac{A\left(1 - e^{-(T - a_n)/\tau}\right)}{T + T_0} + B$.

c. Dependence of $\bar{c}$ and $\bar{s}$ on a_n: We fix T but vary a_n to obtain the dependence of $\bar{c}$ and $\bar{s}$ on a_n (lower panels in Fig. 5). For large a_n, $\bar{c}$ and $\bar{s}$ exhibit linear dependence on a_n, i.e., $A + Ba_n$. For small a_n, they follow $\left(1 - Ce^{-(a_n + D)/\tau}\right)$. We give the specific functions fitted from the simulation data for each case in the Fig. 5 caption, which are in the following form: $(A + Ba_n)\left(1 - Ce^{-(a_n + D)/\tau}\right)$. However, for simplicity and arguments mentioned below, we set $C = 1$ and $D = 0$ for the functions we construct. This choice allows that when $a_n \to 0$, $\bar{c}$ and $\bar{s}$ approach their quiescent state values (see below).

Based on the information above, we construct the following explicit functions for $\bar{c}$ and $\bar{s}$:

$$\bar{c} = u(T, a_n, s_n) = \frac{(\gamma_{c0} + \gamma_c a_n)}{T + T_c}\left(1 - e^{-a_n/\tau_{ac}}\right)\left(1 - e^{-(T - a_n)/\tau_{dc}}\right) + \delta(s_n - \Delta) + c_0,$$

(14)

$$\bar{s} = w(T, a_n) = \frac{(\gamma_{s0} + \gamma_s a_n)}{T + T_s}\left(1 - e^{-a_n/\tau_{as}}\right)\left(1 - e^{(T - a_n)/\tau_{ds}}\right) + s_0,$$

(15)

When $T \to \infty$, or $a_n \to 0$, or $d_n = (T - a_n) \to 0$, $\bar{c} \to \delta(s_0 - \Delta) + c_0$ and $\bar{s} \to s_0$, which correspond to the steady-state values of $\left[\text{Ca}^{2+}\right]_i$ and $\left[\text{Na}^+\right]_i$ of a quiescent cell. Equations (14) and (15) will be used for simulations of the IM model in this study.

3. Determining the dependence of a_n on c_n and s_n—We then seek the functional dependence of a_n on c_n and s_n. In general, one can define $a_n = g(d_{n-1}, c_n, s_n)$, i.e., APD depends not only on ion concentrations but also on diastolic interval. Here, we assume that at slow pacing, the ion channels completely recover at each beat, and thus a_n is independent of d_{n-1} but only a function of c_n and s_n, i.e.,

$$a_n = g(c_n, s_n).$$

(16)

Since $g(c_n, s_n)$ is a two-variable function depending on both c_n and s_n, it becomes nontrivial to be defined. To gain insights into how a_n depends on c_n and s_n, we carry out simulations using random initial conditions for s_n, c_n, and c_{SR}, and measure the quantities many beats later to avoid transient effects. We plot a_n (color map) versus c_n and s_n in Fig. 6(a), a_n versus s_n in Fig. 6(b), and a_n versus c_n in Fig. 6(c). Although the plots are scattered, as shown in the color map, the boundaries between two color scales (iso-APD contour lines) are almost linear, indicating that c_n and s_n are constrained with a linear relationship. Therefore, one can introduce a variable z_n with the following linear transformation:

$$z_n = s_n + \alpha c_n,$$

(17)

and then use this transformation to reduce the two-variable function Eq. (16) into a one-variable one, i.e.,

$$a_n = g(z_n).$$

(18)

Figure 6(d) replots the data in Figs. 6(a)–6(c) using the transformation $z_n = s_n + 43000c_n$, which causes the data points to fall in a very narrow band. A linear fit of the transformed data gives rise to $a_n = 402 - 9.2z_n$. Therefore, with the linear transformation, we can reduce the two-variable function into a one-variable function, and we will show later that the linear transformation works well under the diseased conditions.

Note that c_n is the diastolic $\left[Ca^{2+}\right]_i$ before each beat, and APD is affected by the Ca^{2+} transient, which is more related to the peak and duration of the Ca^{2+} transient. These properties are more causally related to SR Ca^{2+} level and the Ca^{2+} release channels (RyRs). One may also seek the functional relation of APD with SR Ca^{2+} concentration (c_{SR}). Using the same data, if one plots c_n against c_{SRn}, they exhibit a linear relationship [Fig. 6(e)]. Therefore, one can use a similar linear transformation, i.e., $z_n = s_n + \alpha c_{SRn}$ to transform the two-variable function into a one-variable function, as shown in Fig. 6(f).

4.   Feedbacks between $\left[Ca^{2+}\right]_i$ and APD and between $\left[Na^+\right]_i$ and APD—

Because APD affects both $\left[Ca^{2+}\right]_i$ and $\left[Na^+\right]_i$, and $\left[Ca^{2+}\right]_i$ and $\left[Na^+\right]_i$ affect APD, feedback loops form between APD and the ion concentrations. Here we describe the feedback loops based on our simulations of the AP model under the three conditions.

a.   Feedback between APD and $\left[Ca^{2+}\right]_i$.: In previous studies [61–66], the couplings between $\left[Ca^{2+}\right]_i$ and APD were referred to as Ca^{2+}-to-APD coupling and APD-to-Ca^{2+} coupling. The APD-to-Ca^{2+} coupling and Ca^{2+}-to-APD coupling form a feedback loop, and depending on the signs of the couplings, the feedback can be negative or positive. For instance, for the original TP04 model, the APD-to-Ca^{2+} coupling is positive since longer APD results in a higher $\left[Ca^{2+}\right]_i$ [Fig. 5(a)], and the Ca^{2+}-to-APD coupling is negative since a higher $\left[Ca^{2+}\right]_i$ gives rise to a shorter APD [Fig. 6(c)]. Therefore, the feedback between $\left[Ca^{2+}\right]_i$ and APD is negative for the original TP04 model. As we will show later, we can change a negative feedback loop between $\left[Ca^{2+}\right]_i$ and APD to a positive one by enhancing NCX, which then alters the dynamics for both the EAD and spike-and-dome cases. Note that the coupling relationship also depends on the pacing period T [65], and we only focus on slow pacing in this study. Note that the Ca^{2+}-to-APD coupling determines the sign of α in the transformation [Eq. (17)], i.e., for negative coupling, $\alpha > 0$, and for positive coupling, $\alpha < 0$. Because the APD-to-Ca^{2+} coupling is always positive ($\left[Ca^{2+}\right]_i$ is higher for a longer

APD; see Fig. 5), then the sign of α determines the sign of the feedback loop, i.e., the feedback is positive if $\alpha < 0$ and negative if $\alpha > 0$.

b.   Feedback between APD and $\left[\mathrm{Na}^+\right]_i$: The feedback loop between $\left[\mathrm{Na}^+\right]_i$ and APD is more complex since the dependence of $\left[\mathrm{Na}^+\right]_i$ on APD is nonmonotonic. For the original TP04 and the spike-and-dome case, $\left[\mathrm{Na}^+\right]_i$ first increases and then decreases with APD. Because we observe that in general APD decreases with $\left[\mathrm{Na}^+\right]_i$ [e.g., Fig. 6(b)], therefore, when APD is small, the feedback is negative, but it becomes positive when APD is large. For the EAD case, $\left[\mathrm{Na}^+\right]_i$ increases with APD, and thus the feedback is always negative. Note that the dependence of $\bar{c}$ and $\bar{s}$ on a_n shown in Fig. 5 are obtained under voltage-clamp conditions, and they may differ from those under free-running conditions.

5.   Using the IM model to capture the memory effects of the original TP04 model—As a first check of the IM model, we examine if the IM model can capture the memory effects of the TP04 model shown in Fig. 3. Figure 7(a) plots the dependence of $\bar{c}$ and $\bar{s}$ on T and APD using Eqs. (14) and (15), which are similar to those in Fig. 5(a). Figure 7(b) uses the IM model [iterating Eqs. (7), (8), (14), (15), and (19)] to simulate the decay of c_n and s_n using the same protocol as in Figs. 4(b) and 4(c), i.e., fixing $a_n = 300$ ms with free-running s_n (upper two panels) and clamped s_n (lower panel). The results are the same as those shown in Figs. 4(b) and 4(c). That is, for free-running s_n, s_n decays exponentially with n but c_n decays biexponentially with n, and for clamped s_n, c_n decays exponentially with n. Figure 7(c) shows a_n, c_n, and s_n versus n for the pacing period switching from $T = 1$ s to $T = 0.5$ s and back to $T = 1$ s with free-running s_n. The IM model gives rise to the same responses of a_n, c_n, and s_n as those in the original TP04 model shown in Fig. 3(a). After s_n is clamped at 12 mM, a_n and c_n exhibit responses similar to those in Fig. 3(c). These results show that the IM model can well capture the properties of the detailed AP model, not only qualitatively but also quantitatively.

C.   Bifurcations and complex dynamics revealed by the IM model

We use the IM model to perform stability analyses and carry out computer simulations to reveal the bifurcations and the mechanisms of the complex APD dynamics.

1.   Linear stability analysis—Note that only two equations of the three equations are free, and one can eliminate a_n by substituting it in Eqs. (7) and (8) with Eq. (16) [or Eq. (18)]. The linearization of Eqs. (7) and (8) around the steady state is

$$\Delta c_{n+1} = \left[1 - \beta_c\left(1 - \frac{\partial \bar{c}}{\partial c_n}\right)\right]\Delta c_n + \beta_c\frac{\partial \bar{c}}{\partial s_n}\Delta s_n,$$

(19)

$$\Delta s_{n+1} = \left[1 - \beta_s\left(1 - \frac{\partial \overline{s}}{\partial s_n}\right)\right] \Delta s_n + \beta_s \frac{\partial \overline{s}}{\partial c_n} \Delta c_n,$$

(20)

where $\frac{\partial \overline{c}}{\partial c_n} = \frac{\partial u}{\partial a_n}\frac{\partial a_n}{\partial c_n}, \frac{\partial \overline{c}}{\partial s_n} = \frac{\partial u}{\partial s_n} + \frac{\partial u}{\partial a_n}\frac{\partial a_n}{\partial s_n}, \frac{\partial \overline{s}}{\partial s_n} = \frac{\partial w}{\partial a_n}\frac{\partial a_n}{\partial s_n}$, and $\frac{\partial \overline{s}}{\partial c_n} = \frac{\partial w}{\partial a_n}\frac{\partial a_n}{\partial c_n}$. Using $a_n = g(z_n)$ and $z_n = s_n + \alpha c_n$, one has $\frac{\partial a_n}{\partial c_n} = \frac{\partial g(z_n)}{\partial z_n}\frac{\partial z_n}{\partial c_n} = \alpha\frac{\partial g(z_n)}{\partial z_n}$ and $\frac{\partial a_n}{\partial s_n} = \frac{\partial g(z_n)}{\partial z_n}\frac{\partial z_n}{\partial s_n} = \frac{\partial g(z_n)}{\partial z_n}$. Denoting $u_a = \frac{\partial u}{\partial a_n}, u_s = \frac{\partial u}{\partial s_n}, w_a = \frac{\partial w}{\partial a_n}$, and $g' = \frac{\partial g(z_n)}{\partial z_n}$, then Eqs. (19) and (20) become

$$\Delta c_{n+1} = [1 - \beta_c(1 - \alpha u_a g')]\Delta c_n + \beta_c(u_s + u_a g')\Delta s_n,$$

(21)

$$\Delta s_{n+1} = [1 - \beta_s(1 - w_a g')]\Delta s_n + \beta_s \alpha w_a g' \Delta c_n.$$

(22)

We rewrite Eqs. (21) and (22) into the vector form, i.e.,

$$\begin{pmatrix} \Delta c_{n+1} \\ \Delta s_{n+1} \end{pmatrix} = \boldsymbol{J}\begin{pmatrix} \Delta c_n \\ \Delta s_n \end{pmatrix},$$

(23)

where $\boldsymbol{J}$ is the Jacobian matrix, i.e.,

$$\boldsymbol{J} = \begin{bmatrix} 1 - \beta_c + \alpha\beta_c u_a g' & \beta_c(u_s + u_a g') \\ \beta_s \alpha w_a g' & 1 - \beta_s + \beta_s w_a g' \end{bmatrix}.$$

(24)

The stability of the steady state and bifurcations can be obtained by the properties of the eigenvalues of $\boldsymbol{J}$ in Eq. (24). However, based on our simulations, there are limitations in choosing the parameters. As shown in Figs. 4 and 5, the values of β_c and β_s are between 0 and 1 and $\beta_s \ll \beta_c$ [Eq. (11)]. The Na^+-to-APD coupling is mainly negative [e.g., APD is a decreasing function of $\left[Na^+\right]_i$ as shown in Fig. 6(b)]. The Ca^{2+}-to-APD coupling can be either positive ($\alpha < 0$, promoted by high NCX activity; see Fig. 13 and Fig. 17) or negative ($\alpha > 0$, promoted by low NCX activity; see Fig. 14 and Fig. 18). The APD-to-Ca^{2+} coupling is positive (red symbols in the lower panels in Fig. 5), i.e., $\overline{c}$ depends positively on a_n, which indicates that $u_a > 0$. $\left[Ca^{2+}\right]_i$ is proportional to $\left[Na^+\right]_i$, i.e., $\overline{c}$ increases with s_n linearly, indicating that $u_s = \delta > 0$ [Fig. 4(d)]. For the EAD condition, APD-to-Na^+ coupling is positive [lower panel in Fig. 5(b)], i.e., $\overline{s}$ increases with a_n, indicating $w_a > 0$. In the control case [Fig. 5(a)] or the spike-and-dome case [Fig. 5(c)], $\overline{s}$ increases and then decreases as a_n increases, which indicates that APD-to-Na^+ coupling can be either positive ($w_a > 0$) or

negative ($w_a < 0$). For $\beta_s \ll \beta_c$, w_a has little effect on the bifurcations and so does the sign of w_a. Therefore, by applying these constraints, the major parameter that determines the dynamics in the AP model is Ca^{2+}-to-APD coupling, i.e., the magnitude and sign of α. The coupling conditions observed in the AP model are listed in Table I. We first perform a general stability analysis but also consider the information or conditions observed in the AP models. We then carry out simulations of the IM model by using the conditions of and functions reconstructed from the AP model to recapitulate the bifurcations and dynamics of the AP model. The corresponding bifurcations and figures of the results are listed in Table I.

Here, we perform a general stability analysis and discuss the bifurcations by considering the parameter information shown in Table I. Defining $\tau = \text{tr}(\boldsymbol{J})$ and $\Delta = \det(\boldsymbol{J})$ to be the trace and determinant of $\boldsymbol{J}$, then the two eigenvalues are

$$\lambda = \left(\tau \pm \sqrt{\tau^2 - 4\Delta}\right)/2.$$

(25)

Using the stability criteria for IMs combined with the information of $\beta_c, \beta_s, u_a, u_s, w_a$, and g' mentioned above, we obtain the bifurcations and the physiological conditions for the occurrence of the bifurcations as follows:

a. $\underline{\tau^2 - 4\Delta < 0, \textit{Hopf bifurcation}.}$: In this case, the eigenvalues are a pair of complex conjugates, i.e., $\lambda = \left[\tau \pm i\sqrt{-(\tau^2 - 4\Delta)}\right]/2$. When $|\lambda| = \sqrt{\Delta} > 1$, instability occurs via a Hopf bifurcation, which leads to the following stability criterion, i.e., when

$$[w_a\beta_s(1 - \beta_c) + u_a\alpha\beta_c(1 - \beta_s) - \beta_s\beta_c u_s w_a\alpha]g' > \beta_c + \beta_s - \beta_c\beta_s,$$

(26)

the steady state is unstable. Because β_c and β_s are between 0 and 1, then $\beta_c + \beta_s > \beta_c\beta_s$ always holds, and thus the right side of Eq. (26) is always positive. This requires the left side of Eq. (26) to be positive to satisfy the stability criterion. Considering the fact that $\beta_s \ll \beta_c$, one can simplify Eq. (26) to $u_a\alpha\beta_c g' > \beta_c$ or

$$u_a\alpha g' > 1.$$

(27)

Because $u_a > 0$ and $g' < 0$, $\alpha < 0$ is required to satisfy Eq. (27). This implies that for the Hopf bifurcation to occur, a positive feedback between APD and $\left[Ca^{2+}\right]_i$ is required. Theoretically, when β_s is large and $w_a < 0$, Eq. (26) can be satisfied when $\alpha \geqslant 0$. In other words, when the feedback between APD and $\left[Na^+\right]_i$ is positive, a positive feedback between APD and $\left[Ca^{2+}\right]_i$ may not be required.

A limit case is when $\beta_s = 0$, corresponding to $\left[\text{Na}^+\right]_i$ being clamped at a constant. Under this condition, the system is reduced from a two-variable system (both s_n and c_n) to a one-variable system (c_n only). The stability criterion, Eq. (27), then becomes the criterion for bistability to occur in the one-variable system. Bistability under clamped $\left[\text{Na}^+\right]_i$ was indeed observed in the AP models in previous studies [20,32] in which Hopf bifurcations occur when $\left[\text{Na}^+\right]_i$ is free running.

In Fig. 8, we plot the stability boundaries for $\beta_s = 0$ (short-dashed line) and $\beta_s = 0.15$ (solid line), showing that a larger β_s requires a steeper $g(z_n)$ for the Hopf bifurcation to occur. This indicates that a faster $\left[\text{Na}^+\right]_i$ accumulation rate suppresses this instability.

b. $\underline{\tau^2 - 4\Delta > 0}$**, period-doubling bifurcation.:** In this case, the two eigenvalues are real and when the smaller one $\lambda = \left(\tau - \sqrt{\tau^2 - 4\Delta}\right)/2 < -1$, or $\tau + 2 < \sqrt{\tau^2 - 4\Delta}$, instability occurs via a period-doubling bifurcation, which leads to the following stability criterion, i.e., when

$$[w_a\beta_s(2 - \beta_c) + u_a\alpha\beta_c(2 - \beta_s) - \beta_s\beta_c u_s w_a\alpha]g' < -(2 - \beta_c)(2 - \beta_s),$$

(28)

the steady state is unstable. Similarly, when $\beta_s \ll \beta_c$, Eq. (28) can be reduced to

$$u_a\alpha\beta_c g' < -2 + \beta_c.$$

(29)

Because the right side of Eq. (28) or Eq. (29) is always negative, $\alpha > 0$ is needed to satisfy the stability criterion, in particular when $\beta_s \ll \beta_c$. $\alpha > 0$ corresponds to the feedback between APD and $\left[\text{Ca}^{2+}\right]_i$ being negative. However, when β_s is large, $\alpha > 0$ may not be always required (e.g., the period-doubling curve for $\beta_s = 0.2$ in Fig. 8 ends at < 0) to satisfy Eq. (28). This is because the feedback between APD and $\left[\text{Na}^+\right]_i$ is generally negative; this negative feedback can play the same role as the one between APD and $\left[\text{Ca}^{2+}\right]_i$ in promoting the period-doubling bifurcation. In Fig. 8, we plot the stability boundaries $\beta_s = 0$ (dashed) and for $\beta_s = 0.2$ (solid). A larger β_s requires a less steep $g(z_n)$ for the period-doubling bifurcation to occur, indicating that a faster $\left[\text{Na}^+\right]_i$ accumulation rate promotes this instability.

c. $\underline{\tau^2 - 4\Delta > 0}$**, saddle-node bifurcation.:** In this case, when the larger of the two eigenvalues $\lambda = \left(\tau + \sqrt{\tau^2 - 4\Delta}\right)/2 > 1$, or $2 - \tau < \sqrt{\tau^2 - 4\Delta}$, instability occurs via a saddle-node bifurcation, leading to the condition

$$(w_a + u_a\alpha + u_s w_a\alpha)g' > 1.$$

(30)

Note that Eq. (30) is independent of β_c and β_s. To satisfy Eq. (30), $\alpha < 0$ is required since $g' < 0$, i.e., this bifurcation is promoted by the positive feedback between APD and $\left[Ca^{2+}\right]_i$. However, theoretically, because $w_a < 0$ can occur, Eq. (30) can be satisfied even when $\alpha > 0$. In other words, when $w_a < 0$, the feedback between APD and $\left[Na^+\right]_i$ becomes positive, and thus it can give rise to the saddle-node bifurcation. The dashed-dotted curve in Fig. 8 is a stability boundary of this bifurcation. The saddle-node bifurcation leads to bistability in the system. Note that this stability boundary can intersect with that of the Hopf bifurcation, and thus one may see bistability or oscillations depending on the choice of the parameters, such as β_s and α.

2. Bifurcations and complex dynamics using a Hill-type function of $g(z_n)$

—To demonstrate the bifurcations predicted by the stability analysis and the complex dynamics induced by the feedback loops and slow ion accumulation, we carry out computer simulations of the IM model [Eqs. (7) and (8)] using the coupling conditions of the EAD case as shown in Table I and a Hill function for Eq. (18), i.e.,

$$a_n = g(z_n) = a_{\min} + \frac{a_{\max} - a_{\min}}{1 + \left(\frac{z_n}{k_d}\right)^h},$$

(31)

where $a_{\max}$ and $a_{\min}$ are the maximum and minimum APD values. h is the Hill coefficient and k_d is the dissociation constant.

Figure 9(a) is a phase diagram showing the unstable regions in the $\alpha - T$ plane. Agreeing with the linear stability analysis, there are two unstable regions: one when $\alpha < 0$ (unstable I) and one when $\alpha > 0$ (unstable II). Note that to maintain the two unstable regions in the same phase diagram as in Fig. 8, we set k_d as function of α, i.e., $k_d = 11.5 + 0.00005\alpha$. The rationale for doing this is as follows. First, in the linear stability analysis shown in Fig. 8, we do not consider the actual steady state and its change with parameters. Second, in the simulations of the detailed AP model, one observes two unstable regions by altering k_{NCX} (see, e.g., Figs. 10 and 15). Changing k_{NCX} alters both α and k_d (see, e.g., Figs. 13 and 14 and Figs. 17 and 18), and k_d is smaller for $\alpha < 0$ than for $\alpha > 0$, agreeing with the way we alter k_d. With a constant k_d, it is difficult to maintain the two unstable regions on the same phase diagram as in Fig. 9(a) without altering another parameter. Figure 9(b) shows bifurcation diagrams across the two unstable regions for $= 2.5$ s. In unstable region I, only periodic oscillatory behavior is observed [Fig. 9(c)]. In unstable region II, period-doubling routes to chaos occur, leading to high periodicity and chaos [Fig. 9(d)]. Comparing to unstable region I, even though APD varies roughly in the same range, the $\left[Ca^{2+}\right]_i$ variation is attenuated and $\left[Na^+\right]_i$ exhibits almost no variation. Agreeing with the linear stability analysis, when the feedback between APD and $\left[Ca^{2+}\right]_i$ is positive ($\alpha < 0$), Hopf bifurcation leading to

oscillatory dynamics occurs. When the feedback between APD and $\left[\mathrm{Ca}^{2+}\right]_i$ is negative ($\alpha > 0$), period-doubling bifurcations leading to high periodicity and chaos occur.

D.   Bifurcations and complex dynamics in the presence of EADs

To demonstrate that the IM model can capture the complex dynamics in the AP model, we first carry out simulations using the AP model under the condition of EADs. Then, we use the function $g(z_n)$ reconstructed from the simulation data to carry out simulations of the IM model to recapture the bifurcations and the APD dynamics. Figure 10 shows bifurcation diagrams plotting a_n, c_n, and s_n versus k_{NCX}(k_{NCX} controls the strength of NCX) for $T = 2.5$ s. There are two unstable regions in the bifurcation diagrams. When k_{NCX} is small (from 0.75 to 1.5 nA/pF), period-doubling routes to chaos occur, intermingled with periodic windows, corresponding to unstable region II in Fig. 9. When k_{NCX} is large (from 2.1 to 5.6 nA/pF), periodic oscillations occur, corresponding to unstable region I in Fig. 9. Also agreeing with the map results shown in Fig. 9, the APD variations are in the same range in the two regions, but the $\left[\mathrm{Ca}^{2+}\right]_i$ and $\left[\mathrm{Na}^+\right]_i$ varations are different. In unstable region II, the $\left[\mathrm{Ca}^{2+}\right]_i$ variation is attenuated, and $\left[\mathrm{Na}^+\right]_i$ exhibits almost no variation.

To show what happens to the APs in the oscillatory regime, we plot a voltage trace for $T = 2.5$ s and $k_{\mathrm{NCX}} = 5$ nA/pF in Fig. 11(a), which shows oscillatory transitions between APs with EADs and APs without EADs. In this trace, an EAD occurs in each AP from 20 to 67.5 s (total 19 beats), and APD is long. No EAD occurs in the APs from 67.5 to 175 s (total 43 beats), and APD is short. The total length of this combined EAD and no EAD phase is 155 s or 62 beats. This repeats as time goes on, giving rise to a periodic oscillatory behavior. Figure 11(b) plots a_n, c_n, and s_n versus beat number n from the same simulation in Fig. 11(a). The period of oscillation is 62 beats (or 155 s). As APD changes from short to long, both c_n and s_n elevate, and as APD changes from long to short, both c_n and s_n decay. Note that c_n responds much faster than s_n to the APD changes. Figure 11(c) shows bifurcation diagrams plotting $a_n c_n$, and s_n versus T, in which the oscillatory behavior occurs between $T = 2.35$ s and $T = 3.4$ s, but stable for smaller or larger T outside this region.

Because c_n is the diastolic $\left[\mathrm{Ca}^{2+}\right]_i$ before each beat, for comparison, we also plot the peak $\left[\mathrm{Ca}^{2+}\right]_i$ on the same panel in Fig. 11(b), which shows almost the same oscillatory characteristics. It is known that peak $\left[\mathrm{Ca}^{2+}\right]_i$ is proportional to SR Ca^{2+} level (c_{SR}), and as shown in Figs. 4(d) and 6(e), at steady state, c_n is proportional to c_{SR_n}. Therefore, c_n is also proportional to peak $\left[\mathrm{Ca}^{2+}\right]_i$.

Figure 12(a) plots a voltage trace in the chaotic regime for $T = 2.5$ s and $k_{\mathrm{NCX}} = 1$ nA/pF, which shows chaotic traistions between APs with EADs and APs without EADs. Figure 12(b) plots a_n, c_n, and s_n versus beat number n from the same simulation, showing chaotic variations. Figure 12(c) shows bifurcation diagrams plotting a_n, c_n, and s_n versus T, in which chaos and high periodicity occur between $T = 2.38$ s and $T = 2.8$ s. In this case, $\left[\mathrm{Na}^+\right]_i$

accumulation plays almost no role. The bifurcations and complex APD dynamics are mainly caused by the negative feedback between APD and $\left[Ca^{2+}\right]_i$. In our previous study [19], we showed that the chaotic dynamics could be well explained by only including $\left[Ca^{2+}\right]_i$ accumulation.

To use the IM model to capture the dynamics of the AP model under the EAD condition, we reconstruct $g(z_n)$ from the simualtion data of the AP model and determine a set of parameters for the functions of $\bar{c}$ and $\bar{s}$ [Eqs. (14) and (15)] based on the c_n and s_n levels measured in the AP model. We first reconstruct a $g(z_n)$ for $k_{NCX} = 5$ nA/pF (oscillatory regime). Figure 13(a) replots all the data from Fig. 11(c) in the forms of a_n against s_n (left) and a_n against c_n (middle). In both plots, the data points are scattered. We then plot a_n against z_n (right) using the transformation $z_n = s_n + \alpha c_n$ with $\alpha = -13000$. This transformation converts the scattered plots into a plot with the data being in a narrow band. We construct a piecewise linear function (solid line in the right panel) for $g(z_n)$ based on this plot. To quantitatively match the bifurcations and the values of c_n and s_n requires a proper set of parameters for the functions of $\bar{c}$ and $\bar{s}$ [Eqs. (14) and (15)]. Because the parameters of the fitting functions in Figs. 4 and 5 are obtained under voltage-clamp conditions, it may differ from the free-running conditions, and thus we cannot directly take them from Figs. 4 and 5. We first determine the ranges of the parameters based on the results in Figs. 4 and 5. We then take the steady-state data from the AP model (e.g., the steady states in the long or short T in the bifurcation diagrams) and iterate the IM model to adjust the parameters to reach the same steady states. However, the choice of the parameters is not unique, and many sets of parameters can meet the criterion equally well. We use one of them for the simulations of the IM model, which are listed in the figure caption for each case.

Using the reconstructed functions, we carry out simulations of the IM model [Eqs. (7) and (8)]. Figure 13(b) plots a_n, c_n, and s_n versus n for $T = 2.5$ s and Fig. 13(c) shows bifurcation diagrams plotting a_n, c_n, and s_n versus T. Oscillatory behavior occurs between $T = 2.36$ s and $= 3.38$ s. The simulation results of the IM model shown in Figs. 13(b) and 13(c) are almost the same as those from the AP model shown in Figs. 11(b) and 11(c). Note that we have to use $\alpha < 0$ to transform the scattered data into a narrow band to reconstruct $g(z_n)$, and this transformation is not arbitrary but unique. This indicates that the feedback between APD and $\left[Ca^{2+}\right]_i$ is positve, and thus the dynamics remains oscillatory as predicted by the theory.

We then repeat the process for the chaotic case shown in Fig. 12. In this case, $\alpha = 25000$ converts the scattered plots into a very narrow-band plot [Fig. 14(a)]. $\alpha > 0$ indicates that the feedback between APD and $\left[Ca^{2+}\right]_i$ is negative and thus the dynamics is chaotic. Again, the simulations of the IM model using the reconstructed $g(z_n)$ give rise to almost the same bifurcations and dynamics [Figs. 14(b) and 14(c)] as those from the AP model shown in Figs. 12(b) and 12(c), capturing the dynamics not only qualitatively but also quantitatively well.

E. Bifurcations and complex dynamics under the condition of spike-and-dome AP morphology

Similar to the EAD case, we first carry out simulations of the AP model under the spike-and-dome AP morphology condition, and then recapture the bifurcations and APD dynamics using the IM model. Differing from the EAD case, in the spike-and-dome case, we find that $[K^+]_i$ cannot reach a steady state under certain parameters in our simulations. This might be the same steady-state issue of cardiac AP models that has been addressed previously [67]. To avoid this, and because $[K^+]_i$ accumulation exhibits only a small effect on APD, $[Na^+]_i$, and $[Ca^{2+}]_i$ (Note this does not mean that $[K^+]_i$ is not important, but as long as it is in the physiological range, its effect on dynamics is small), we clamp $[K^+]_i = 136$ mM for all simulations in this case. With some changes in parameters of the original TP04 model and substitution of I_{to} (see Sec. II), we observe the same complex dynamics as in the EAD case. Figure 15(a) shows bifurcation diagrams plotting a_n, c_n, and s_n versus k_{NCX} for $T = 1.6$ s. When $k_{NCX} < 1.2$ nA/pF, the system is stable. For $k_{NCX} = 1.2$ to 4.2 nA/pF, chaos intermingling with periodic windows occurs. In this regime, the variation of c_n is small, and that of s_n is negligible. When $k_{NCX} > 4.2$ nA/pF, oscillatory behavior occurs. In this regime, the variations of c_n and s_n are large. Figure 15(b) shows bifurcation diagrams plotting a_n, c_n, and s_n versus T for $k_{NCX} = 5$ nA/pF, which is in the oscillatory regime. The oscillatory behavior occurs between $T = 1280$ ms and $= 1850$ ms. Figure 15(c) shows bifurcation diagrams plotting a_n, c_n, and s_n versus T for $k_{NCX} = 3$ nA/pF, which is in the chaotic regime. Chaos and high periodicity occur for > 1360 ms. Figure 16 shows example traces of voltage [Figs. 16(a) and 16(b)] and the corresponding a_n, c_n, and s_n versus n for the oscillatory [Fig. 16(c)] and chaotic [Fig. 16(d)] regimes.

Following the same procedure as in the EAD case, we reconstruct $g(z_n)$ and choose parameters for the functions of $\bar{c}$ and $\bar{s}$ [Eqs. (14) and (15)] for the two cases shown in Figs. 15(b) and 15(c). Figure 17(a) replots the data in Fig. 15(b) in the forms of a_n against s_n (left) and a_n against c_n (middle), showing two scattered plots. We then plot a_n against z_n (right) using the transform $z_n = s_n + \alpha c_n$ with $\alpha = -22\,000$, tranforming the scattered plots into a narrow-band plot. $\alpha < 0$ indicates that the feedback between APD and $[Ca^{2+}]_i$ is positive and the dynamics shall be osillatory. Using the reconstructed $g(z_n)$ [red curve in the right panel in Fig. 17(a)], and a proper set of parameters for the fucntions of $\bar{c}$ and $\bar{s}$ [Eqs. (14) and (15)] for the IM model, we obtain almost the same bifurcation diagrams [Fig. 17(b)] and oscillatory behavior [Fig. 17(c)] as the ones from the AP model shown in Figs. 15(b) and 16(c).

We repeat the same process for the chaotic case. Figure 18(a) replots the data from Fig. 15(c) in the forms of a_n against s_n (left) and a_n against c_n (middle), showing two scattered plots. We then plot a_n against z_n (right) using the transformation $z_n = s_n + \alpha c_n$ with $\alpha = 250\,000$, transforming the scattered plots into a very narrow-band plot. $\alpha > 0$ indicates that the feedback between APD and $[Ca^{2+}]_i$ is negative and the dynamics shall be chaotic. Using the

reconstructed $g(z_n)$ [red curve in the right panel in Fig. 18(a)], and a proper set of parameters for $\bar{c}$ and $\bar{s}$ [Eqs. (14) and (15)] for the IM model, we also obtain almost the same bifurcation diagrams [Fig. 18(b)] and chaotic behavior [Fig. 18(c)] as the ones from the AP model shown in Figs. 15(c) and 16(d).

IV. DISCUSSION AND CONCLUSIONS

In this study, we investigate the roles of ion accumulation in the genesis of complex APD dynamics using computer simulations of a detailed AP model under two different diseased conditions and develop an IM model to reveal the underlying dynamical mechanisms. We first use simulation of the detailed AP model under normal condition to inform the development of the IM equations and construction of the IM functions for the IM model. We then validate the IM model using simulations of the detailed AP model under two diseased conditions in which complex APD dynamics occur. Our major observations from simulations of the detailed AP model and theoretical analyses of the IM model are the following: (1) The occurrence of EADs or spike-and-dome AP morphology results in a steep dependence of APD on ion concentrations (as well as other parameters, e.g., ion channel conductance), and this steep dependence is required for the occurrence of the complex AP dynamics; (2) When the feedback between $\left[Ca^{2+}\right]_i$ and APD is positive, a Hopf bifurcation leading to oscillatory APD behavior occurs. When the feedback is negative, period-doubling bifurcations leading to high periodicity and chaos occur; (3) The slow accumulation of $\left[Na^+\right]_i$ and its negative feedback with APD are required for the Hopf bifurcation but not for the period-doubling bifurcations; (4) Using functions constructed using simulation data from the detailed AP model, the two-dimensional IM model cannot only qualitatively but also quantitatively capture the bifurcations and APD dynamics of the detailed high-dimensional AP model. Moreover, the IM model can explicitly dissect out the roles of the feedback loops and the APD responses to the changes of the ion concentrations in the genesis of the complex dynamics, unifying the two dynamical regimes under the same theoretical framework; and (5) Although the underlying diseased conditions or causes of the spike-and-dome case are different from those of the EAD case, the dynamical mechanisms for the complex APD dynamics are identical, which can be captured by the same IM model.

It is known that slow ion accumulation is the main contributor for short-term memory in the heart [33,68]. Short-term memory has been investigated in many previous theoretical studies [11,18,69–71] which incorporated phenomenologically a "memory" variable in the models. Our IM model incorporates the specific feedback loops and timescales of $\left[Ca^{2+}\right]_i$ and $\left[Na^+\right]_i$ accumulation, linking short-term memory and slow ion accumulation to the genesis of complex APD dynamics in ventricular myocytes under diseased conditions. In particular, the roles of the feedback loops between APD and ion concentrations in generating the bifurcations and nonlinear dynamics are explicitly dissected out in the IM model.

It is shown that both EADs and spike-and-dome AP morphology can generate early spontaneous excitations in cardiac tissue, called premature ventricular complexes (PVCs) via dynamical instabilities [55,72]. These PVCs may propagate into longer APD regions

to result in reentry via unidirectional conduction block [73] or degenerate directly into reentry [46]. The dynamics revealed in this study may provide mechanistic insights beyond the generation of reentry. First, cellular chaos may synchronize at the tissue scale [44,74] to result in dynamical dispersion of refractoriness or multifocal arrhythmias. Second, the cellular oscillatory behavior may directly manifest at the tissue as Torsade de Pointes or nonsustained ventricular tachycardia that occur and terminate spontaneously [75–77]. Nevertheless, how these dynamics are manifested at the tissue scale and what new tissue-scale dynamics may emerge from them need to be investigated in future studies.

In the current IM model, although both $\left[\mathrm{Ca}^{2+}\right]_i$ and $\left[\mathrm{Na}^+\right]_i$ play important roles in generating the complex dynamics, the instability is still driven by the steep change in APD in response to the changes of the ion concentrations, i.e., the steep decreasing $g(z_n)$ in the IM model. This instability is still a voltage-driven one. It is well known that dynamical instabilities can occur in the Ca^{2+} cycling system itself, independent of the voltage system [63,65,78–82]. It is known that coupling between APD and Ca^{2+} can bring in novel dynamics when both systems are unstable [61,62,64,66]. We will integrate our previous IM models [64,82] with the IM model in this study to form an IM model that couples the voltage-driven and Ca^{2+}-driven dynamics as well as the short-term memory caused by ion accumulation to investigate the nonlinear dynamics emerging in cardiac systems.

In conclusion, slow ion accumulation, in particular $\left[\mathrm{Na}^+\right]_i$ accumulation, plays a major role in short-term cardiac memory. Their memory effects combined with their feedback loops with APD can generate complex APD dynamics under diseased conditions. These complex dynamics can be well described by a low-dimensional IM model incorporating $\left[\mathrm{Ca}^{2+}\right]_i$ and $\left[\mathrm{Na}^+\right]_i$ accumulation and the feedbacks between APD and $\left[\mathrm{Ca}^{2+}\right]_i$ and $\left[\mathrm{Na}^+\right]_i$. Furthermore, the same IM model unifies the bifurcations and complex dynamics under different dynamical regimes and different diseased conditions into a single theoretical framework, providing a theoretical tool for analyzing the dynamical mechanisms of complex dynamics in cardiac myocytes.

ACKNOWLEDGMENTS

References

[1]. Winfree AT, Sudden cardiac death: A problem in topology, Sci. Am 248, 144 (1983). [PubMed: 6857229]

[2]. Glass L, Dynamics of cardiac arrhythmias, Phys. Today 49, 40 (1996).

[3]. Qu Z, Hu G, Garfinkel A, and Weiss JN, Nonlinear and stochastic dynamics in the heart, Phys. Rep 543, 61 (2014). [PubMed: 25267872]

[4]. Karma A and Gilmour RF, Nonlinear dynamics of heart rhythm disorders, Phys. Today 60, 51 (2007).

[5]. Krogh-Madsen T and Christini DJ, Nonlinear dynamics in cardiology, Annu. Rev. Biomed. Eng 14, 179 (2012). [PubMed: 22524390]

[6]. Qu Z and Weiss JN, Mechanisms of ventricular arrhythmias: From molecular fluctuations to electrical turbulence, Annu. Rev. Physiol 77, 29 (2015). [PubMed: 25340965]

[7]. Qu Z and Weiss JN, Cardiac alternans: From bedside to bench and back, Circ. Res 132, 127 (2023). [PubMed: 36603066]

[8]. Özgen N and Rosen MR, Cardiac memory: A work in progress, Heart Rhythm 6, 564 (2009). [PubMed: 19324320]

[9]. Kalb SS, Dobrovolny HM, Tolkacheva EG, Idriss SF, Krassowska W, and Gauthier DJ, The restitution portrait: A new method for investigating rate-dependent restitution, J. Cardiovasc. Electrophysiol 15, 698 (2004). [PubMed: 15175067]

[10]. Franz MR, Swerdlow CD, Liem LB, and Schaefer J, Cycle length dependence of human action potential duration in vivo: Effects of single extrastimuli, sudden sustained rate acceleration and deceleration, and different steady-state frequencies, J. Clin. Invest 82, 972 (1988). [PubMed: 3417875]

[11]. Fox JJ, Bodenschatz E, and Gilmour RF, Period-doubling instability and memory in cardiac tissue, Phys. Rev. Lett 89, 138101 (2002). [PubMed: 12225067]

[12]. Cherry EM and Fenton FH, Suppression of alternans and conduction blocks despite steep APD restitution: Electrotonic, memory and conduction velocity restitution effects, Am. J. Physiol. Heart Circ. Physiol 286, H2332 (2004). [PubMed: 14751863]

[13]. Gilmour RF, Otani NF, and Watanabe MA, Memory and complex dynamics in cardiac Purkinje fibers, Am. J. Physiol. Heart Circ. Physiol 41, H1826 (1997).

[14]. Li M and Otani NF, Ion channel basis for alternans and memory in cardiac myocytes, Ann. Biomed. Eng 31, 1213 (2003). [PubMed: 14649495]

[15]. Baher A, Qu Z, Hayatdavoudi A, Lamp ST, Yang MJ, Xie F, Turner S, Garfinkel A, and Weiss JN, Short-term cardiac memory and mother rotor fibrillation, Am. J. Physiol. Heart Circ. Physiol 292, H180 (2007). [PubMed: 16891403]

[16]. Kim TY, Hong JH, Heo R, and Lee KJ, Alternans by non-monotonic conduction velocity restitution, bistability and memory, New J. Phys 15, 013046 (2013).

[17]. Mironov S, Jalife J, and Tolkacheva EG, Role of conduction velocity restitution and short-term memory in the development of action potential duration alternans in isolated rabbit hearts, Circulation 118, 17 (2008). [PubMed: 18559701]

[18]. Landaw J, Garfinkel A, Weiss JN, and Qu Z, Memory-induced chaos in cardiac excitation, Phys. Rev. Lett 118, 138101 (2017). [PubMed: 28409990]

[19]. Landaw J and Qu Z, Memory-induced nonlinear dynamics of excitation in cardiac diseases, Phys. Rev. E 97, 042414 (2018). [PubMed: 29758700]

[20]. Landaw J and Qu Z, Bifurcations caused by feedback between voltage and intracellular ion concentrations in ventricular myocytes, Phys. Rev. Lett 123, 218101 (2019). [PubMed: 31809131]

[21]. Zeng J, Laurita KR, Rosenbaum DS, and Rudy Y, Two components of the delayed rectifier K^+ current in ventricular myocytes of the guinea pig type. Theoretical formulation and their role in repolarization, Circ. Res 77, 140 (1995). [PubMed: 7788872]

[22]. Pelzmann B, Schaffer P, Bernhart E, Lang P, Mächler H, Rigler B, and Koidl B, L-type calcium current in human ventricular myocytes at a physiological temperature from children with tetralogy of Fallot, Cardiovasc. Res 38, 424 (1998). [PubMed: 9709403]

[23]. Nie A and Meng Z, Modulation of L-type calcium current in rat cardiac myocytes by sulfur dioxide derivatives, Food Chem. Toxicol 44, 355 (2006). [PubMed: 16182427]

[24]. Wang X, Gao G, Guo K, Yarotskyy V, Huang C, Elmslie KS, and Peterson BZ, Phospholemman modulates the gating of cardiac L-type calcium channels, Biophys. J 98, 1149 (2010). [PubMed: 20371314]

[25]. Hille B, Ion Channels of Excitable Membranes (Sinauer Associates, Inc., Sunderland, Massachusetts, 2001).

[26]. Keener JP and Sneyd J, Mathematical Physiology (Springer, New York, 1998).

[27]. Del Negro CA, Hsiao CF, Chandler SH, and Garfinkel A, Evidence for a novel bursting mechanism in rodent trigeminal neurons, Biophys. J 75, 174 (1998). [PubMed: 9649377]

[28]. Shilnikov A, Calabrese RL, and Cymbalyuk G, Mechanism of bistability: Tonic spiking and bursting in a neuron model, Phys. Rev. E 71, 056214 (2005).

[29]. Kunysz AM, Shrier A, and Glass L, Bursting behavior during fixed-delay stimulation of spontaneously beating chick heart cell aggregates, Am. J. Physiol. Cell Physiol 273, C331 (1997).

[30]. Torrente AG, Zhang R, Zaini A, Giani JF, Kang J, Lamp ST, Philipson KD, and Goldhaber JI, Burst pacemaker activity of the sinoatrial node in sodium–calcium exchanger knockout mice, Proc. Natl. Acad. Sci. USA 112, 9769 (2015). [PubMed: 26195795]

[31]. Glynn P, Onal B, and Hund TJ, Cycle length restitution in sinoatrial node cells: A theory for understanding spontaneous action potential dynamics, PLoS One 9, e89049 (2014). [PubMed: 24533169]

[32]. Xie Y, Liao Z, Grandi E, Shiferaw Y, and Bers DM, Slow [Na]i changes and positive feedback between membrane potential and [Ca]i underlie intermittent early afterdepolarizations and arrhythmias, Circ. Arrhythm. Electrophysiol 8, 1472 (2015). [PubMed: 26407967]

[33]. Krogh-Madsen T and Christini DJ, Slow $\left[\mathrm{Na}^+\right]_i$ dynamics impacts arrhythmogenesis and spiral wave reentry in cardiac myocyte ionic model, Chaos 27, 093907 (2017). [PubMed: 28964146]

[34]. ten Tusscher KH, Noble D, Noble PJ, and Panfilov AV, A model for human ventricular tissue, Am. J. Physiol. Heart Circ. Physiol 286, H1573 (2004). [PubMed: 14656705]

[35]. Morita H, Wu J, and Zipes DP, The QT syndromes: Long and short, Lancet North Am. Ed 372, 750 (2008).

[36]. Roden DM, Drug-induced prolongation of the QT interval, N. Engl. J. Med 350, 1013 (2004). [PubMed: 14999113]

[37]. Tomaselli GF and Marban E, Electrophysiological remodeling in hypertrophy and heart failure, Cardiovasc. Res 42, 270 (1999). [PubMed: 10533566]

[38]. Tran DX, Sato D, Yochelis A, Weiss JN, Garfinkel A, and Qu Z, Bifurcation and chaos in a model of cardiac early afterdepolarizations, Phys. Rev. Lett 102, 258103 (2009). [PubMed: 19659123]

[39]. Qu Z, Xie L-H, Olcese R, Karagueuzian HS, Chen P-S, Garfinkel A, and Weiss JN, Early afterdepolarizations in cardiac myocytes: Beyond reduced repolarization reserve, Cardiovasc. Res 99, 6 (2013). [PubMed: 23619423]

[40]. Clancy CE and Rudy Y, Linking a genetic defect to its cellular phenotype in a cardiac arrhythmia, Nature (London) 400, 566 (1999). [PubMed: 10448858]

[41]. Vandersickel N, Kazbanov IV, Nuitermans A, Weise LD, Pandit R, and Panfilov AV, A study of early afterdepolarizations in a model for human ventricular tissue, PLoS One 9, e84595 (2014). [PubMed: 24427289]

[42]. Pueyo E, Corrias A, Virag L, Jost N, Szel T, Varro A, Szentandrassy N, Nanasi PP, Burrage K, and Rodriguez B, A multiscale investigation of repolarization variability and its role in cardiac arrhythmogenesis, Biophys. J 101, 2892 (2011). [PubMed: 22208187]

[43]. Sato D, Xie LH, Nguyen TP, Weiss JN, and Qu Z, Irregularly appearing early afterdepolarizations in cardiac myocytes: Random fluctuations or dynamical chaos? Biophys. J 99, 765 (2010). [PubMed: 20682253]

[44]. Sato D, Xie LH, Sovari AA, Tran DX, Morita N, Xie F, Karagueuzian H, Garfinkel A, Weiss JN, and Qu Z, Synchronization of chaotic early afterdepolarizations in the genesis of cardiac arrhythmias, Proc. Natl. Acad. Sci. USA 106, 2983 (2009). [PubMed: 19218447]

[45]. Barrio R, Martínez MÁ, Serrano S, and Pueyo E, Dynamical mechanism for generation of arrhythmogenic early afterdepolarizations in cardiac myocytes: Insights from in silico electrophysiological models, Phys. Rev. E 106, 024402 (2022). [PubMed: 36109976]

[46]. Qu Z, Liu MB, Olcese R, Karagueuzian H, Garfinkel A, Chen P-S, and Weiss JN, R-on-T and the initiation of reentry revisited: Integrating old and new concepts, Heart Rhythm 19, 1369 (2022). [PubMed: 35364332]

[47]. Antzelevitch C, The Brugada syndrome: Ionic basis and arrhythmia mechanisms, J. Cardiovasc. Electrophysiol 12, 268 (2001). [PubMed: 11232628]

[48]. Wilde AAM, Postema PG, Di Diego JM, Viskin S, Morita H, Fish JM, and Antzelevitch C, The pathophysiological mechanism underlying Brugada syndrome: Depolarization versus repolarization, J. Mol. Cell Cardiol 49, 543 (2010). [PubMed: 20659475]

[49]. Di Diego JM and Antzelevitch C, Pinacidil-induced electrical heterogeneity and extrasystolic activity in canine ventricular tissues. Does activation of ATP-regulated potassium current promote phase 2 reentry? Circulation 88, 1177 (1993). [PubMed: 7689041]

[50]. Di Diego JM and Antzelevitch C, High $\left[Ca^{2+}\right]o$-induced electrical heterogeneity and extrasystolic activity in isolated canine ventricular epicardium. Phase 2 reentry, Circulation 89, 1839 (1994). [PubMed: 7511994]

[51]. Lukas A and Antzelevitch C, Phase 2 reentry as a mechanism of initiation of circus movement reentry in canine epicardium exposed to simulated ischemia, Cardiovasc. Res 32, 593 (1996). [PubMed: 8881520]

[52]. Maoz A, Christini DJ, and Krogh-Madsen T, Dependence of phase-2 reentry and repolarization dispersion on epicardial and transmural ionic heterogeneity: A simulation study, Europace 16, 458 (2014). [PubMed: 24569901]

[53]. Maoz A, Krogh-Madsen T, and Christini DJ, Instability in action potential morphology underlies phase 2 reentry: A mathematical modeling study, Heart Rhythm 6, 813 (2009). [PubMed: 19467510]

[54]. Zhang Z, Chen P-S, Weiss JN, and Qu Z, Why is only type 1 electrocardiogram diagnostic of Brugada syndrome? Mechanistic insights from computer modeling, Circ. Arrhythm. Electrophysiol 15, e010365 (2022). [PubMed: 34963310]

[55]. Zhang Z and Qu Z, Life and death saddles in the heart, Phys. Rev. E 103, 062406 (2021). [PubMed: 34271754]

[56]. Lukas A and Antzelevitch C, Differences in the electrophysiological response of canine ventricular epicardium and endocardium to ischemia. Role of the transient outward current, Circulation 88, 2903 (1993). [PubMed: 8252704]

[57]. Landaw J, Yuan X, Chen P-S, and Qu Z, The transient outward potassium current plays a key role in spiral wave breakup in ventricular tissue, Am. J. Physiol. Heart Circ. Physiol 320, H826 (2021). [PubMed: 33385322]

[58]. Hodgkin AL and Huxley AF, A quantitative description of membrane current and its application to conduction and excitation in nerve, J. Physiol 117, 500 (1952). [PubMed: 12991237]

[59]. Huang X, Kim TY, Koren G, Choi B-R, and Qu Z, Spontaneous initiation of premature ventricular complexes and arrhythmias in type 2 long QT syndrome, Am. J. Physiol. Heart Circ. Physiol 311, H1470 (2016). [PubMed: 27765749]

[60]. Mahajan A, Shiferaw Y, Sato D, Baher A, Olcese R, Xie L-H, Yang M-J, Chen P-S, Restrepo JG, Karma A et al. , A rabbit ventricular action potential model replicating cardiac dynamics at rapid heart rates, Biophys. J 94, 392 (2008). [PubMed: 18160660]

[61]. Shiferaw Y, Sato D, and Karma A, Coupled dynamics of voltage and calcium in paced cardiac cells, Phys. Rev. E 71, 021903 (2005).

[62]. Sato D, Shiferaw Y, Garfinkel A, Weiss JN, Qu Z, and Karma A, Spatially discordant alternans in cardiac tissue. Role of calcium cycling, Circ. Res 99, 520 (2006). [PubMed: 16902177]

[63]. Shiferaw Y and Karma A, Turing instability mediated by voltage and calcium diffusion in paced cardiac cells, Proc. Natl. Acad. Sci. USA 103, 5670 (2006). [PubMed: 16574775]

[64]. Qu Z, Shiferaw Y, and Weiss JN, Nonlinear dynamics of cardiac excitation-contraction coupling: An iterated map study, Phys. Rev. E 75, 011927 (2007).

[65]. Song Z and Qu Z, Delayed global feedback in the genesis and stability of spatiotemporal excitation patterns in paced biological excitable media, PLoS Comput. Biol 16, e1007931 (2020). [PubMed: 33017392]

[66]. Huang C, Song Z, and Qu Z, Synchronization of spatially discordant voltage and calcium alternans in cardiac tissue, Phys. Rev. E 106, 024406 (2022). [PubMed: 36109882]

[67]. Hund TJ, Kucera JP, Otani NF, and Rudy Y, Ionic charge conservation and long-term steady state in the Luo-Rudy dynamic cell model, Biophys. J 81, 3324 (2001). [PubMed: 11720995]

[68]. Faber GM and Rudy Y, Action potential and contractility changes in [Na(+)](i) overloaded cardiac myocytes: A simulation study, Biophys. J 78, 2392 (2000). [PubMed: 10777735]

[69]. Otani NF, Theory of the development of alternans in the heart during controlled diastolic interval pacing, Chaos 27, 093935 (2017). [PubMed: 28964128]

[70]. Tolkacheva EG, Schaeffer DG, Gauthier DJ, and Krassowska W, Condition for alternans and stability of the 1:1 response pattern in a "memory" model of paced cardiac dynamics, Phys. Rev. E 67, 031904 (2003).

[71]. Otani NF and Gilmour RF, Memory models for the electrical properties of local cardiac systems, J. Theor. Biol 187, 409 (1997). [PubMed: 9245581]

[72]. Zhang Z, Liu MB, Huang X, Song Z, and Qu Z, Mechanisms of premature ventricular complexes caused by QT prolongation, Biophys. J 120, 352 (2021). [PubMed: 33333033]

[73]. Qu Z, Garfinkel A, and Weiss JN, Vulnerable window for conduction block in a one-dimensional cable of cardiac cells, 1: Single extrasystoles, Biophys. J 91, 793 (2006). [PubMed: 16679367]

[74]. de Lange E, Xie Y, and Qu Z, Synchronization of early afterdepolarizations and arrhythmogenesis in heterogeneous cardiac tissue models, Biophys. J 103, 365 (2012). [PubMed: 22853915]

[75]. Cranefield PF and Aronson RS, Torsade de Pointes and other pause-induced ventricular tachycardias: The short-long-short sequence and early afterdepolarizations, Pacing. Clin. Electrophysiol 11, 670 (1988). [PubMed: 2456546]

[76]. Leenhardt A, Glaser E, Burguera M, Nurnberg M, Maison-Blanche P, and Coumel P, Short-coupled variant of torsade de pointes. A new electrocardiographic entity in the spectrum of idiopathic ventricular tachyarrhythmias, Circulation 89 1, 206 (1994). [PubMed: 8281648]

[77]. Vandersickel N, Bossu A, De Neve J, Dunnink A, Meijborg VMF, van der Heyden MAG, Beekman JDM, De Bakker JMT, Vos MA, and Panfilov AV, Short-lasting episodes of Torsade de Pointes in the chronic atrioventricular block dog model have a focal mechanism, while longer-lasting episodes are maintained by re-entry, JACC: Clinical Electrophysiology 3, 1565 (2017). [PubMed: 29759839]

[78]. Diaz ME, O'Neill SC, and Eisner DA, Sarcoplasmic reticulum calcium content fluctuation is the key to cardiac alternans, Circ. Res 94, 650 (2004). [PubMed: 14752033]

[79]. Li Y, Diaz ME, Eisner DA, and O'Neill S, The effects of membrane potential, SR Ca^{2+} content and RyR responsiveness on systolic Ca^{2+} alternans in rat ventricular myocytes, J. Physiol 587, 1283 (2009). [PubMed: 19153161]

[80]. Picht E, DeSantiago J, Blatter LA, and Bers DM, Cardiac alternans do not rely on diastolic sarcoplasmic reticulum calcium content fluctuations, Circ. Res 99, 740 (2006). [PubMed: 16946134]

[81]. Shiferaw Y, Watanabe MA, Garfinkel A, Weiss JN, and Karma A, Model of intracellular calcium cycling in ventricular myocytes, Biophys. J 85, 3666 (2003). [PubMed: 14645059]

[82]. Qu Z, Liu MB, and Nivala M, A unified theory of calcium alternans in ventricular myocytes, Sci. Rep 6, 35625 (2016). [PubMed: 27762397]
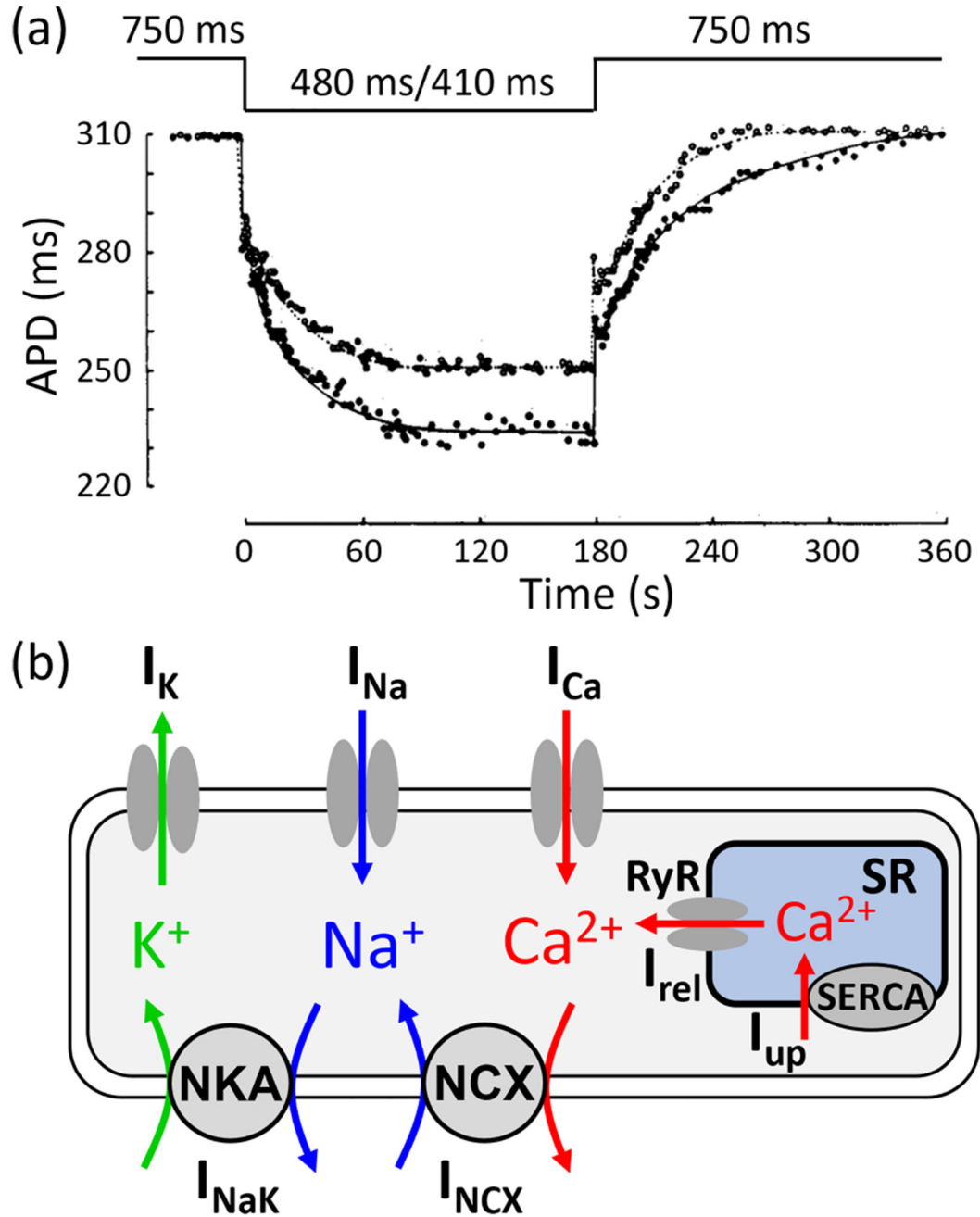
FIG. 1.

Cardiac memory and intracellular ion accumulation. (a) Responses of APD to sudden changes (as marked) of pacing period in a human heart, modified from Franz *et al.* (Ref. [10]). (b) Schematic plot of ion cycling between intracellular and extracellular space via membrane ion channels and pumps. K^+ enters the cell via NKA and extrudes via the K^+ channel. Na^+ enders the cell via the Na^+ channel and NCX, and extrudes via NKA. Ca^{2+} enters the cell via the Ca^{2+} channel and extrudes via NCX. Ca^{2+} also has an internal cycle, which is key to contraction of the heart. In this cycle, Ca^{2+} releases from the SR via the

RyRs on the SR membrane and is reup taken back into the SR via the SERCA pump. SR is the major Ca^{2+} store in a myocyte.
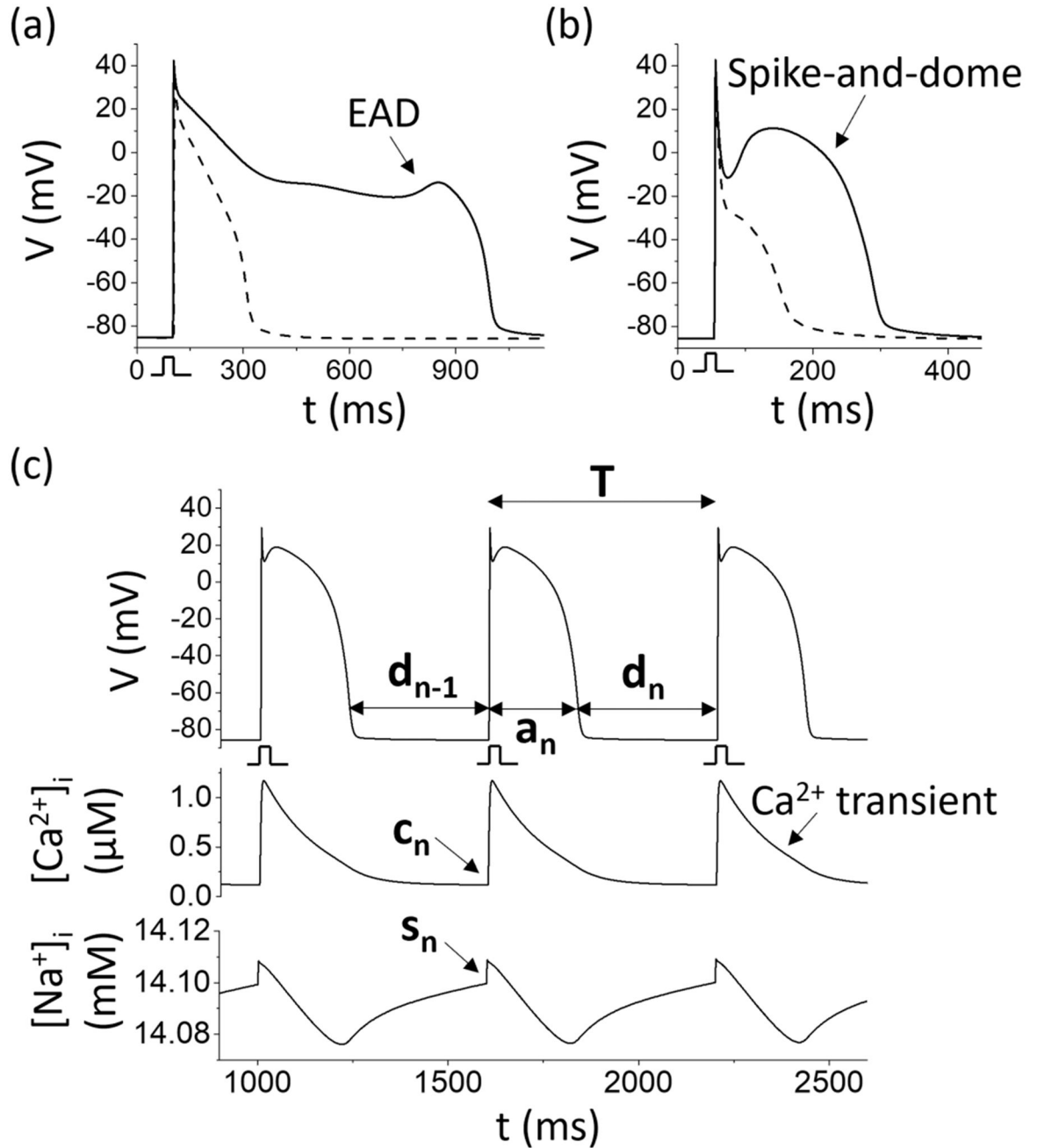
FIG. 2.

APs under disease conditions and definition of variables for the IM model. (a) An AP with a low $I_{C,L}$ and no EAD (dashed, $G_{Ca,L} = 0.000035 \mathrm{cm^3}/ \mu \mathrm{F/s}$) and one with a high $I_{Ca,L}$ and EAD (solid, $G_{Ca,L} = 0.00014 \mathrm{cm^3}/ \mu \mathrm{F/s}$) from the AP model of the EAD case. The cyan mark indicates the square-pulse stimulus, which is given at = 100 ms. (b) A spike-and-dome AP with an intermediate I_{to} (solid, $G_{to} = 0.19$ mS/cm^2) and a spike AP with a high I_{to} (dashed, $G_{to} = 0.3$ mS/cm^2) from the AP model of the spike-and-dome case. (c) Example traces of

$V, \left[\text{Ca}^{2+} \right]_i$, and $\left[\text{Na}^+ \right]_i$ vs time from the original TP04 model under periodic pacing with a period of T. a_n is the APD of the nth beat, which is defined as the time duration when $V \geq -75\text{mV}$. d_n is the diastolic interval of the nth beat [d_{n-1} for the $(n-1)$th beat], which is defined as the time duration when $V < -75\text{mV}$. c_n and s_n are the values of $\left[\text{Ca}^{2+} \right]_i$ and $\left[\text{Na}^+ \right]_i$ measured at the moment before the stimulus is given for the nth beat. In physiology, the $\left[\text{Ca}^{2+} \right]_i$ trace during an AP is also called a Ca^{2+} transient.
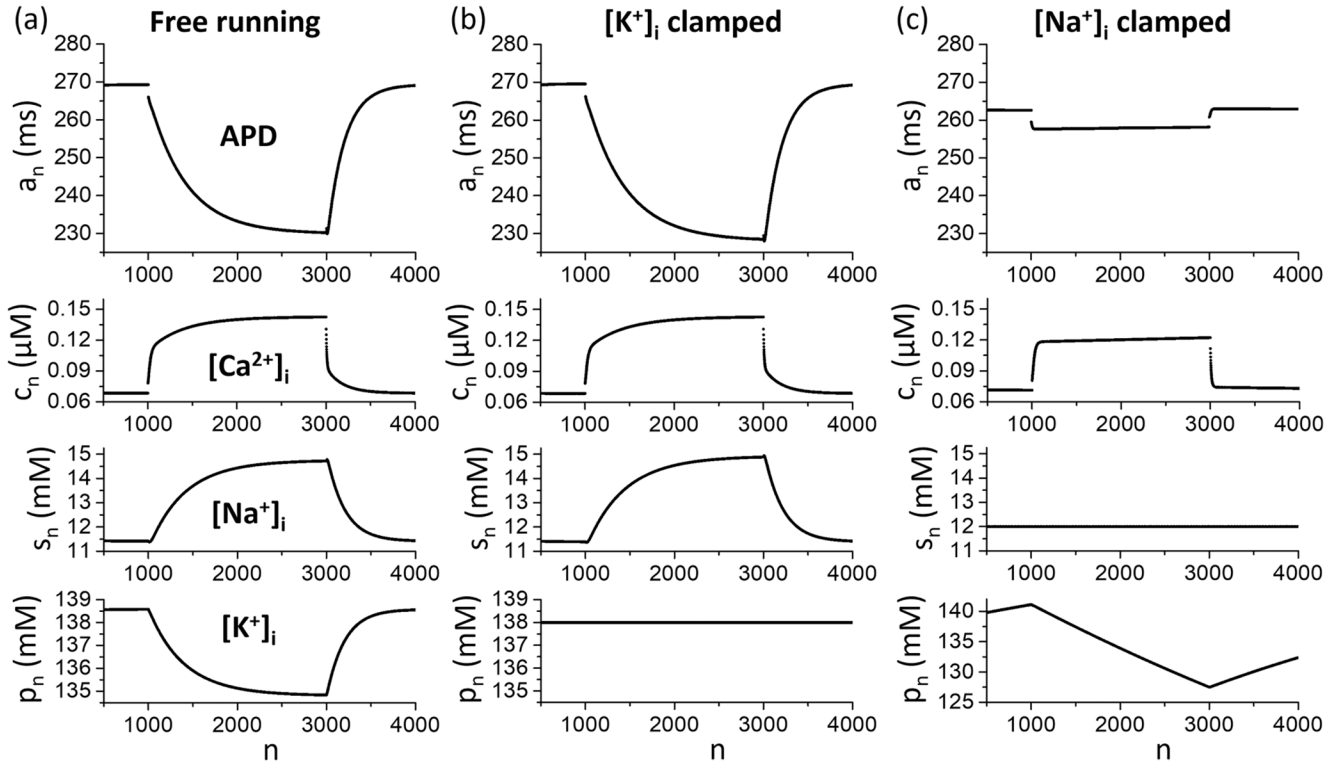
FIG. 3.

Responses of APD, $\left[Ca^{2+}\right]_i$, $\left[Na^+\right]_i$, and $\left[K^+\right]_i$ to sudden changes of pacing period T in the original TP04 model. (a) a_n, c_n, s_n, and p_n (diastolic $\left[K^+\right]_i$ right before each beat) vs beat number n in a simulation in which T is switched from $T = 1$ s to $T = 0.5$ s and back to $T = 1$ s. (b) Same as (a) but $\left[K^+\right]_i$ is clamped at $\left[K^+\right]_i = 138$ mM. (c) Same as (a) but $\left[Na^+\right]_i$ is clamped at $\left[Na^+\right]_i = 12$ mM.
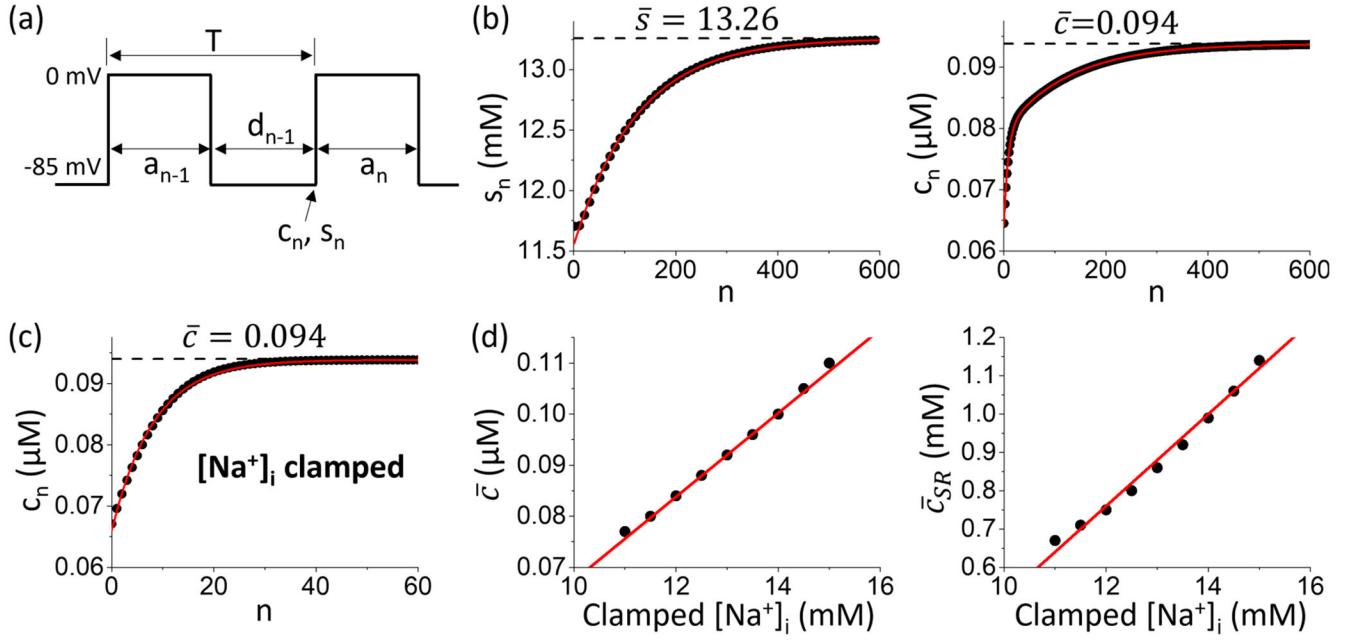
FIG. 4.

$\left[Ca^{2+}\right]_i$ and $\left[Na^+\right]_i$ behaviors under voltage-clamp conditions. (a) Schematic plot of the voltage-clamp protocol. T is the period, a_n is APD, and d_n is the diastolic interval. c_n and s_n are the values at the time when the voltage is changed from -85 to 0 mV. (b) Left: s_n vs n starting from an initial condition away from its steady-state value $\bar{s}$. $a_n = a = 300$ ms and $= 1.5$ s. The line is a single-exponential fit: $s_n = 13.26 - 1.71e^{-n/124.2}$ mM. Right: c_n vs n from the same simulation. The line is a biexponential fit: $c_n = \left(94 - 16e^{-n/8.1} - 14e^{-n/127.8}\right) \times 10^{-6}$ mM. (c) c_n vs n for $\left[Na^+\right]_i$ clamped at 13.26 mM. The line is a single-exponential fit: $c_n = \left(94 - 28e^{-n/8.1}\right) \times 10^{-6}$ mM. (d) Left: $\bar{c}$ vs clamped $\left[Na^+\right]_i$. The line is a linear fit: $\bar{c} = \left(-14.6 + 8.2\bar{s}\right) \times 10^{-6}$ mM. Right: $\bar{c}_{SR}$ vs clamped $\left[Na^+\right]_i$. The line is a linear fit: $\bar{c}_{SR} = -0.68 + 0.12\bar{s}$ mM.
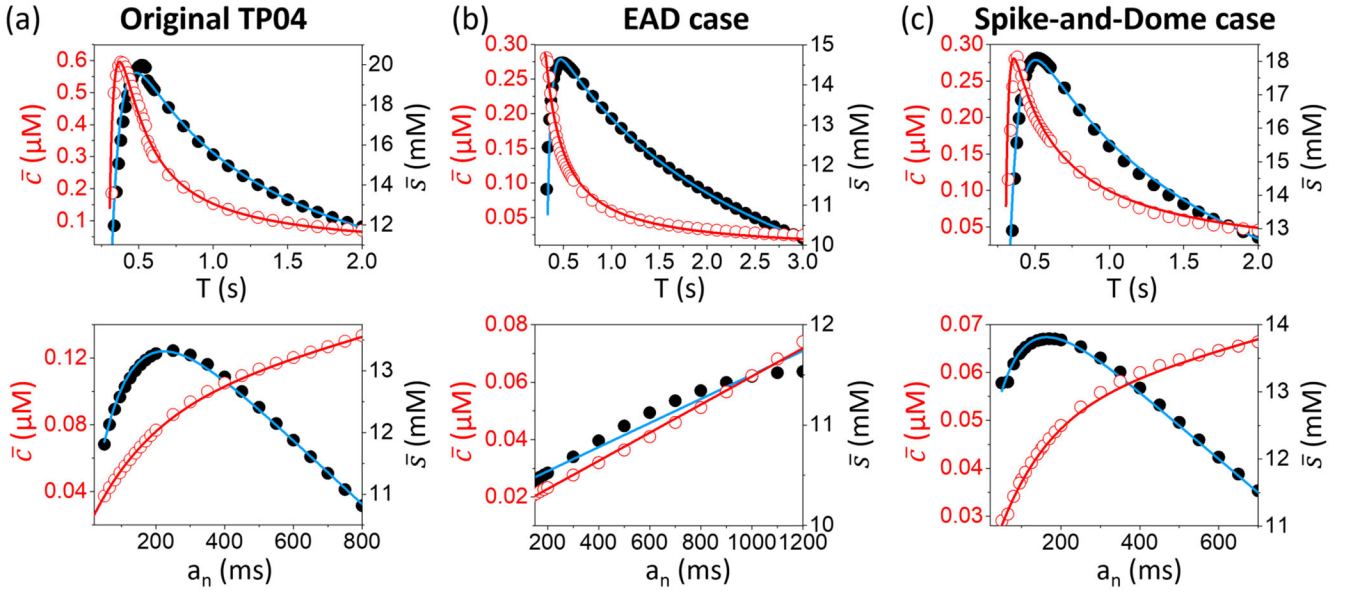
FIG. 5.

Dependences of $\bar{c}$ and $\bar{s}$ on T and a_n under different conditions. Solid ($\bar{s}$) and open ($\bar{c}$) circles are simulation data using the same voltage-clamp protocol as in Fig. 4(a) and lines are plots of the corresponding fitting functions. (a) Original TP04 model. Upper: $\bar{c}$ and $\bar{s}$ vs T for $a_n = 300$ ms. $\bar{c}$ and $\bar{s}$ were taken at the 1200th beat for each T. The fitting functions are $\bar{c} = 0.115\left(1 - e^{-(T-300)/72}\right)/\left(T - 250\right)$ mM and $\bar{s} = 6.2 + \frac{14300}{T + 520}\left(1 - e^{-(T-300)/60}\right)$ mM. Lower: $\bar{c}$ and $\bar{s}$ vs a_n for $= 1500$ ms. The fitting functions are $\bar{c} = (87 + 0.058a_n)\left(1 - 0.8e^{-a_n/160}\right) \times 10^{-6}$ mM and $\bar{s} = (15 - 0.0052a_n)\left(1 - 0.4e^{-(a_n + 25)/105}\right)$ mM. (b) The EAD case with $k_{NCX} = 3$ nA/pF. Upper: $\bar{c}$ and $\bar{s}$ vs T for $a_n = 300$ ms. The fitting functions are $\bar{c} = 0.055\left(1 - e^{-(T-300)/1.5}\right)/\left(T - 120\right)$ mM and $\bar{s} = 5.7 + \frac{22400}{T + 2000}\left(1 - e^{-(T-300)/40}\right)$ mM. Lower: $\bar{c}$ and $\bar{s}$ vs a_n for $= 2500$ ms. The fitting functions are $\bar{c} = (13 + 0.049a_n)\left(1 - e^{-a_n/2.2}\right) \times 10^{-6}$ mM and $\bar{s} = (10.3 + 0.0012a_n)\left(1 - e^{-a_n/1.5}\right)$ mM. (c) The spike-and-dome case with $k_{NCX} = 3$ nA/pF. Upper: $\bar{c}$ and $\bar{s}$ vs T for $a_n = 300$ ms. The fitting functions are $\bar{c} = 0.096\left(1 - e^{-(T-300)/20}\right)/\left(T - 35\right)$ mM and $\bar{s} = 6.95 + 17\,085\left(1 - e^{-(T-300)/65}\right)/\left(T + 970\right)$ mM. Lower: $\bar{c}$ and $\bar{s}$ vs a_n for $= 1600$ ms. The fitting functions are $\bar{c} = (51 + 0.023a_n)\left(1 - 0.7e^{-a_n/120}\right) \times 10^{-6}$ mM and $\bar{s} = (15 - 0.005a_n)\left(1 - 0.32e^{-(a_n + 25)/75}\right)$ mM.
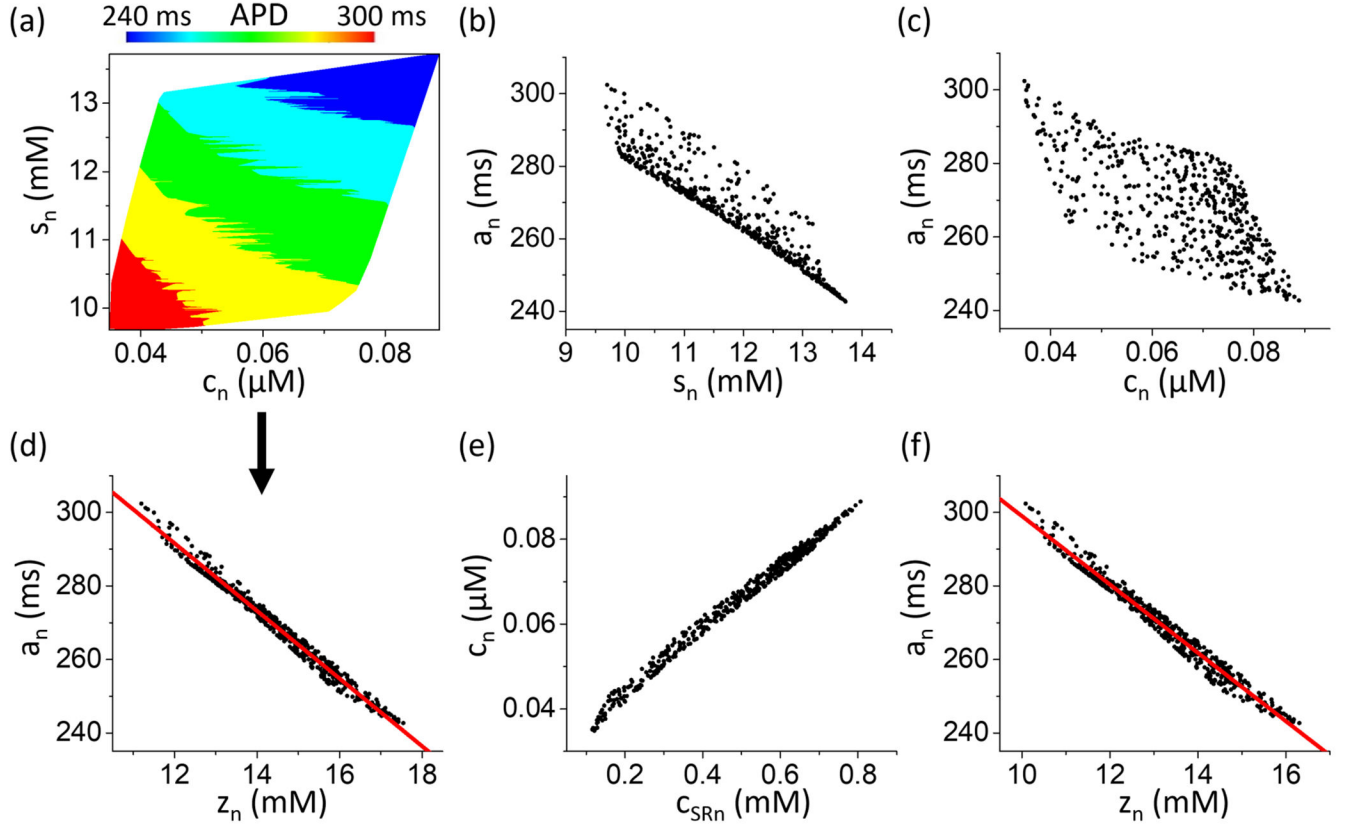
FIG. 6.

Transforming a two-variable function into a one-variable function for the original TP04 model. (a) Color map of a_n vs c_n and s_n. At $t = 0$ (after the system reaches steady state), $\left[Ca^{2+}\right]_i$, $\left[Na^+\right]_i$, and $\left[Ca^{2+}\right]_{SR}$ are reset randomly by drawing from the intervals $[0.00005, 0.00009]$, $[9.75, 13.75]$, and $[0, 1]$ mM, respectively. The cell is paced with $= 1$ s, and c_n, s_n, and c_{SRn} are taken at the end of beat No. 10. (b) a_n vs s_n from the same dataset. (c) APD vs c_n from the same dataset. (d) a_n vs z_n after the transformation $z_n = s_n + 43000c_n$. The straight line is a linear fit with the following function: $a_n = 402 - 9.2z_n$. (e) c_n vs c_{SRn} from the same dataset. (f) a_n vs z_n using the transformation $z_n = s_n + 3.2c_{SRn}$. The straight line is a linear fit with the following function: $a_n = 392 - 9.3z_n$.
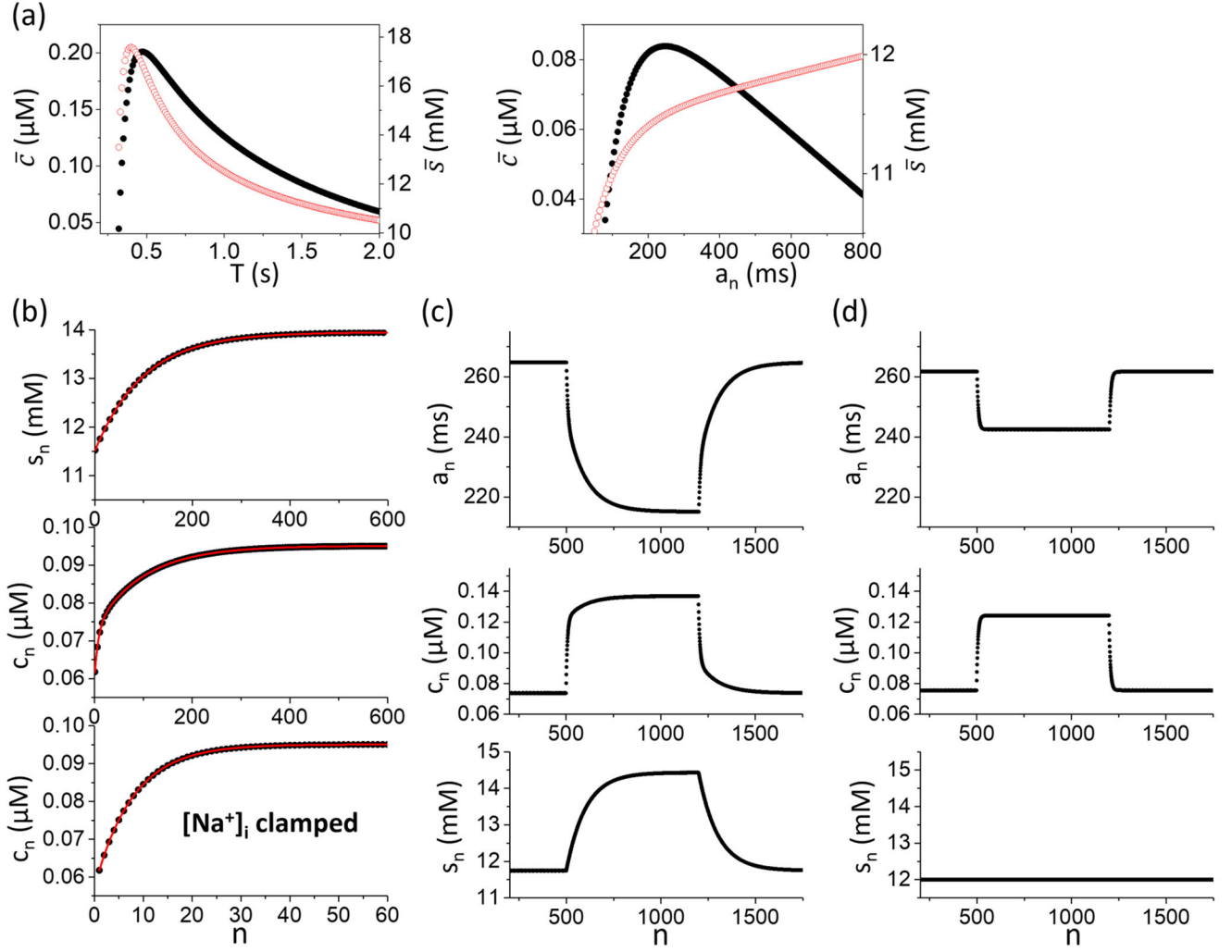
FIG. 7.

Memory effects simulated using the IM model. (a) $\bar{c}$ (open circles) and $\bar{s}$ (solid circles) vs T with $a_n = 300$ ms (left) and $\bar{c}$ and $\bar{s}$ vs a_n with $T = 1$ s using Eqs. (14) and (15) with the following parameters: $\gamma_{c0} = 0.0075, \gamma_c = 0.000058, \tau_{ac} = 100, \tau_{dc} = 70, T_c = -250, \delta = 8.2 \times 10^{-6}, \Delta = 6.2, c_0 = 0, \gamma_{s0} = 13500, \gamma_s = -5.2, \tau_{as} = 70, \tau_{ds} = 60, s_0 = 6.2$, and $T_s = 520 \cdot \beta_c = 0.12$ and $\beta_s = 0.01$. These parameters are either the same as or similar to the ones in the fitting functions in Fig. 5(a) for the original TP04 model [Note: due to T in the denominator in Eqs. (14) and (15) being in the order of 1000, the γ values are 1000-fold of the corresponding values in the fitting functions in the lower panel in Fig. 5(a)]. (b) Simulating the voltage-clamp condition with $a_n = 300$ ms and $T = 1$ s in the IM model. Upper and middle panels: c_n and s_n vs n. The lines are exponential fits: $s_n = 13.95 - 2.45e^{-n/99.5}$ mM and $c_n = \left(95 - 13e^{-n/7.8} - 22e^{-n/99.5}\right) \times 10^{-6}$ mM. Lower panel: c_n vs n when s_n is clamped at 13.95 mM. The same functions of $\bar{c}$ and $\bar{s}$ as in (a) are used. The line is an exponential fit: $c_n = \left(95 - 38e^{-n/7.8}\right) \times 10^{-6}$ mM. (c) Simulating the memory effect in the IM model. a_n, c_n, and s_n vs n for T changes from 1 s ($n < 500$)

to 0.5 $s(500 < n < 1200)$ and back to 1 $s(n > 1200)$. (d) Same as (c) but s_n is clamped at 12 mM. For (c) and (d), the same functions for $\bar{c}$ and $\bar{s}$ as in (a) are used except $\gamma_{s0} = 10000$. $a_n = g(z_n) = 402 - 9.2z_n$ and $z_n = s_n + 43000c_n$ are used.
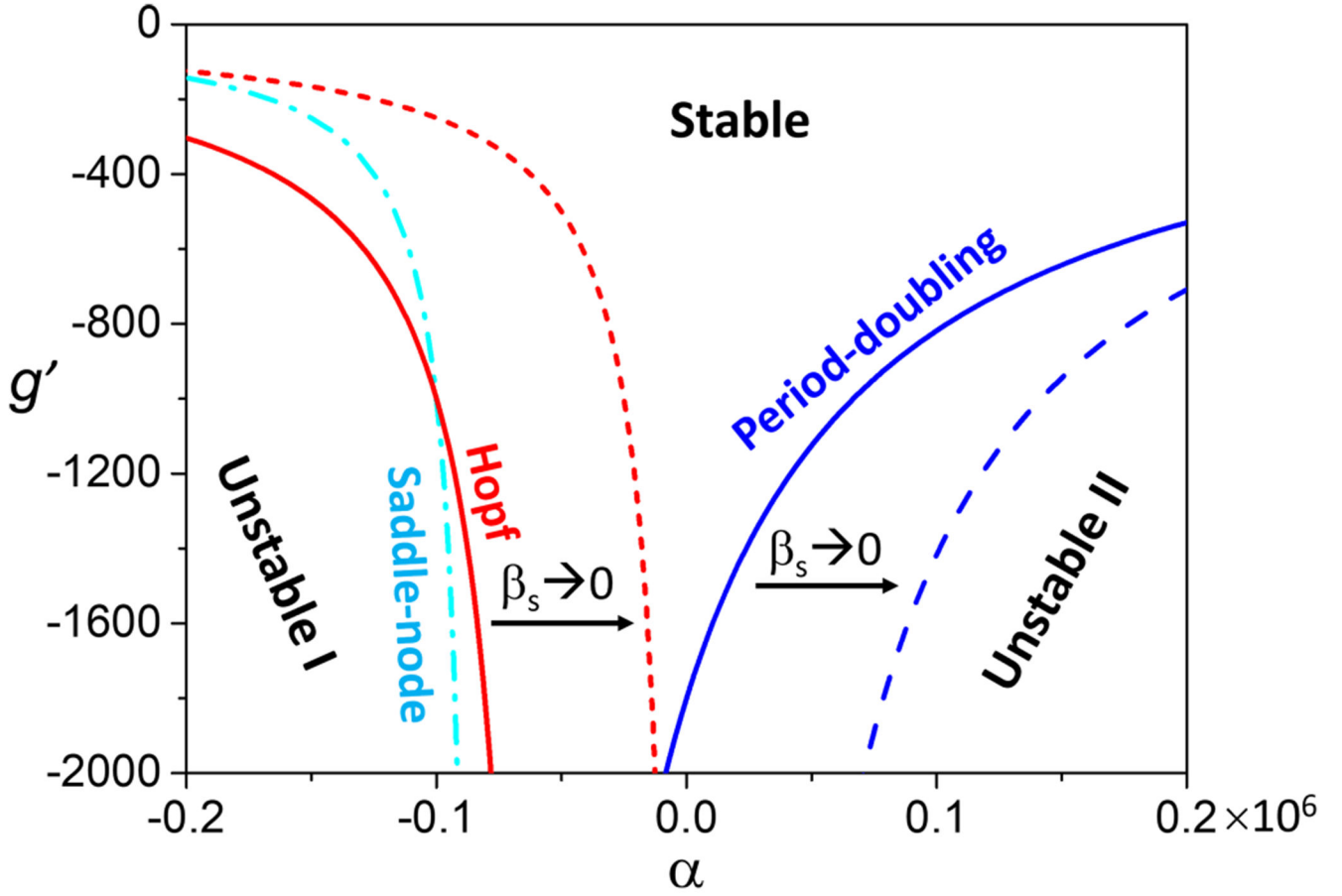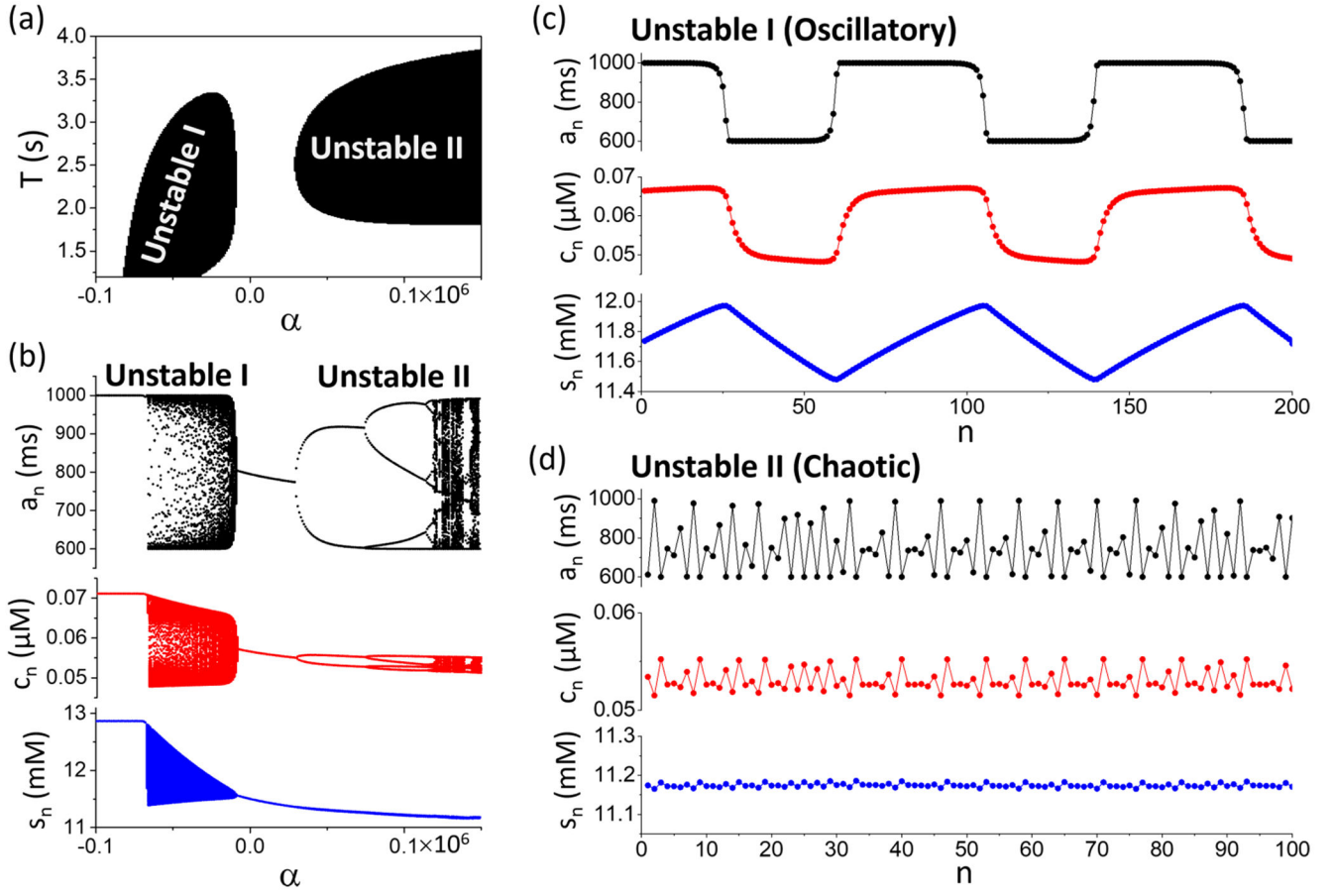
FIG. 8.

Stability boundaries of the steady state in the $g' - \alpha$ space from the IM model.

$u_s = \delta = 4 \times 10^{-6}$, $u_a = 0.04 \times 10^{-6}$, $w_a = 0.005$, and $\beta_c = 0.3$. Period-doubling bifurcations for $\beta_s = 0.2$ (solid) and $\beta_s \to 0$ (dashed). Hopf bifurcations for $\beta_s = 0.15$ (solid) and $\beta_s \to 0$ (short dashed). Saddle-node bifurcation (dashed-dotted). The steady state is stable above but unstable below these boundaries.

FIG. 9.

Bifurcations and complex dynamics of the IM model with a Hill $g(z_n)$ function. (a) Phase diagram showing the unstable regions in $\alpha - T$ space. (b) Bifurcation diagrams showing a_n, c_n, and s_n vs α for $T = 2.5$ s. (c) An example of oscillatory behavior from unstable region I with $\alpha = -0.03 \times 10^6$. (d) An example of chaotic behavior from unstable region II with $\alpha = 0.132 \times 10^6$. The parameters for the functions of $\bar{c}$ and $\bar{s}$ [Eqs. (14) and (15)] are $\gamma_{c0} = 0$, $\gamma_c = 0.0002$, $\tau_{ac} = 2.2$, $\tau_{dc} = 1.5$, $T_c = 2000$, $\delta = 4 \times 10^{-6}$, $\Delta = 6.2$, $c_0 = 0$, $\gamma_{s0} = 0$, $\gamma_s = 30$, $\tau_{as} = 1.5$, $\tau_{ds} = 40$, $s_0 = 6.2$, and $T_s = 2000$. The parameters for the Hill function [Eq. (31)] are $a_{max} = 1000$ ms, $a_{min} = 600$ ms, $h = 500$, and $k_d = 11.5 + 0.00005\alpha$. $\beta_c = 0.3$ and $\beta_s = 0.01$.
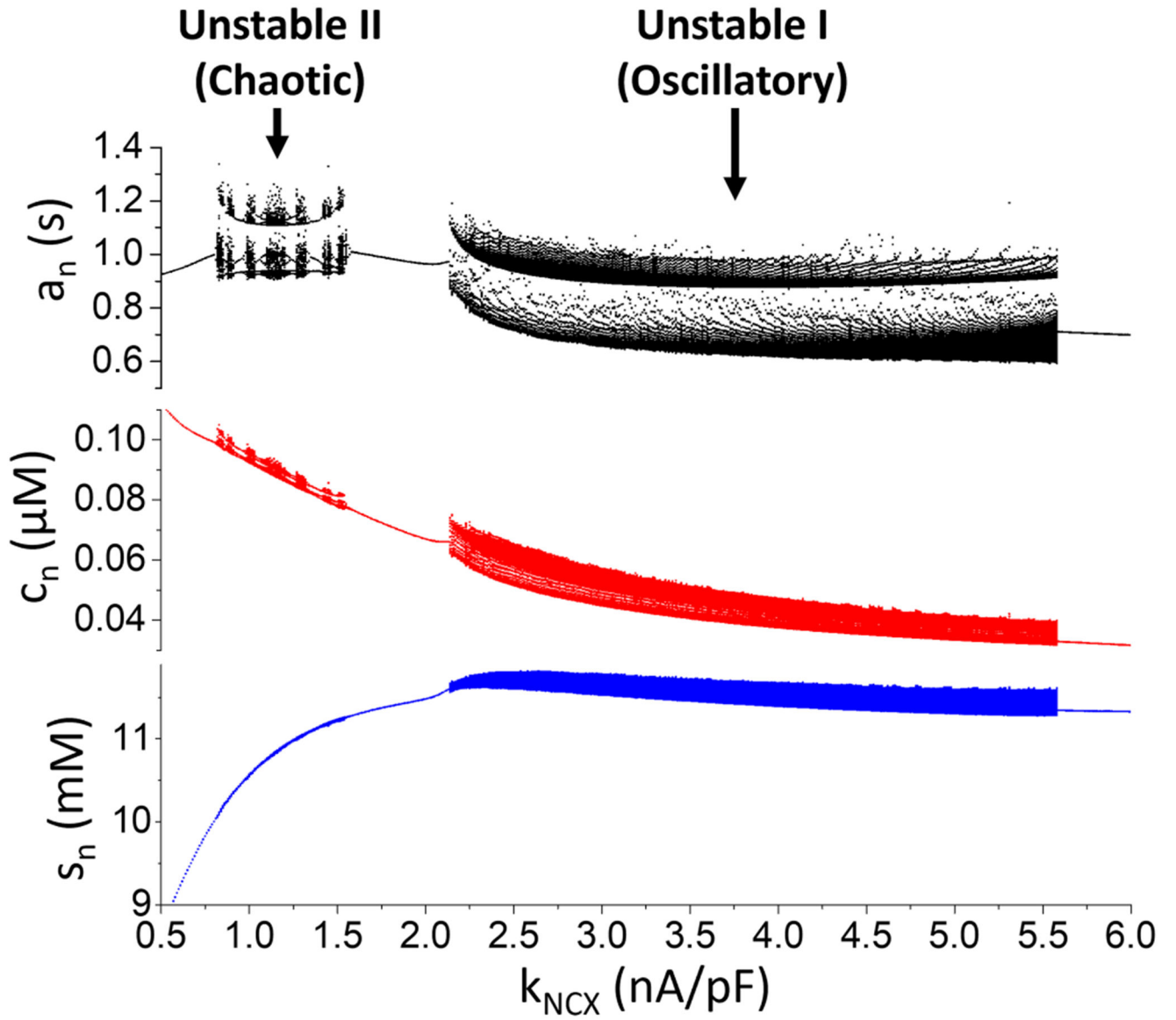
FIG. 10.

Bifurcations and complex APD dynamics in the AP model under the EAD condition. Plotted are a_n, c_n, and s_n vs k_{NCX} for $T = 2.5$ s.
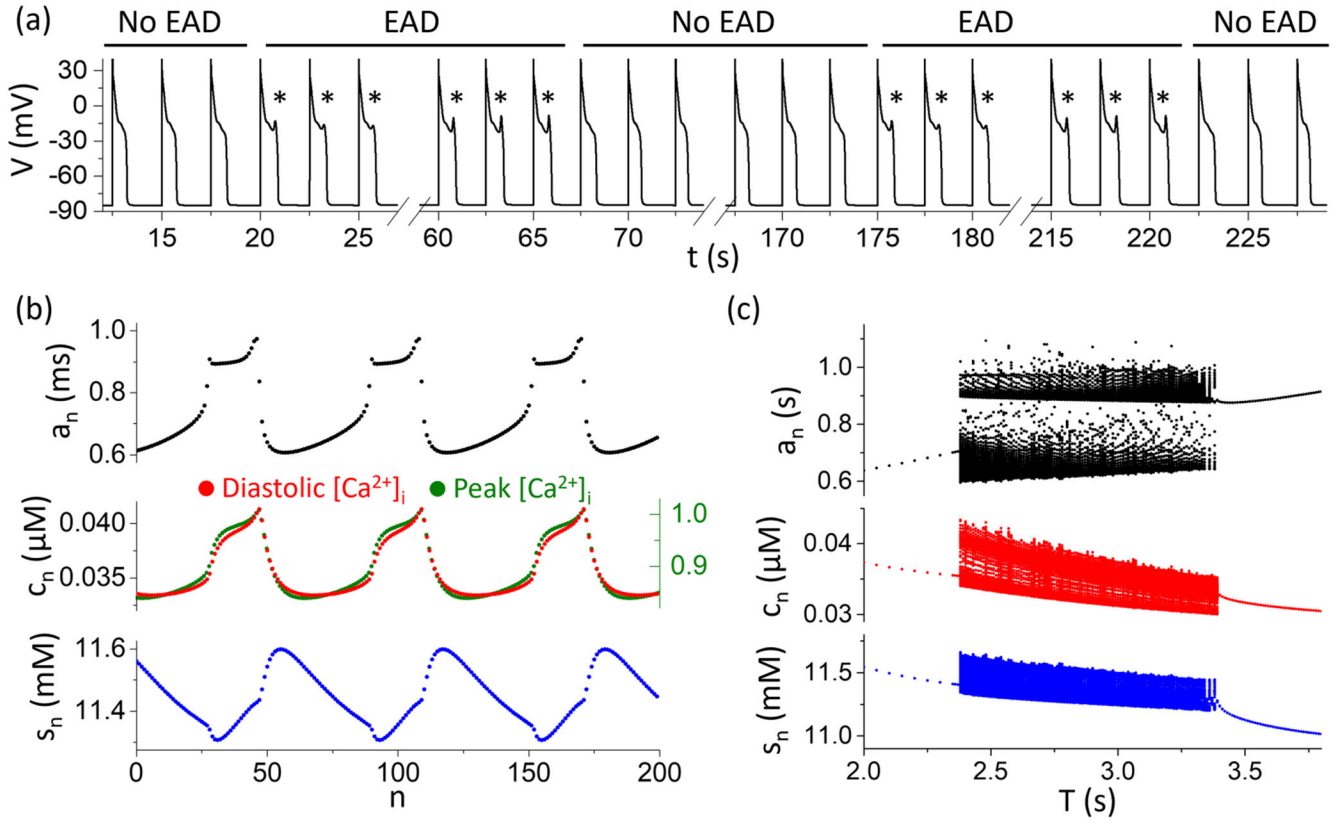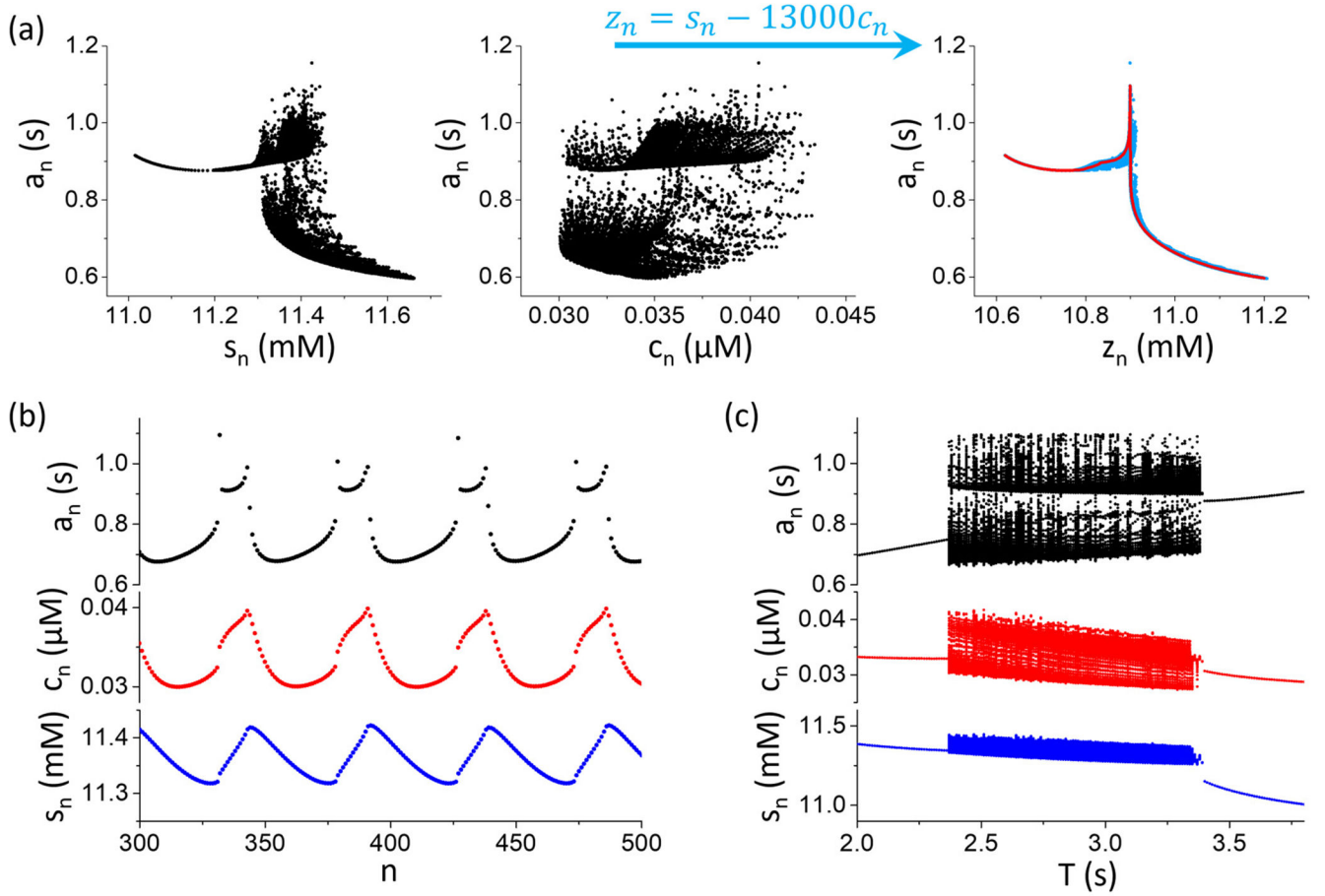
FIG. 11.

Oscillatory behaviors in the AP model under the EAD condition. (a) Voltage trace showing oscillatory transition between APs with EADs and APs without EADs. The symbol * marks the APs with EADs. $T = 2.5$ s and $k_{NCX} = 5$ nA/pF. (b) a_n, c_n(and peak $\left[Ca^{2+}\right]_i$), and s_n vs n from the same simulation in (a). (c) Bifurcation diagrams showing a_n, c_n, and s_n vs T for $k_{NCX} = 5$ nA/pF.
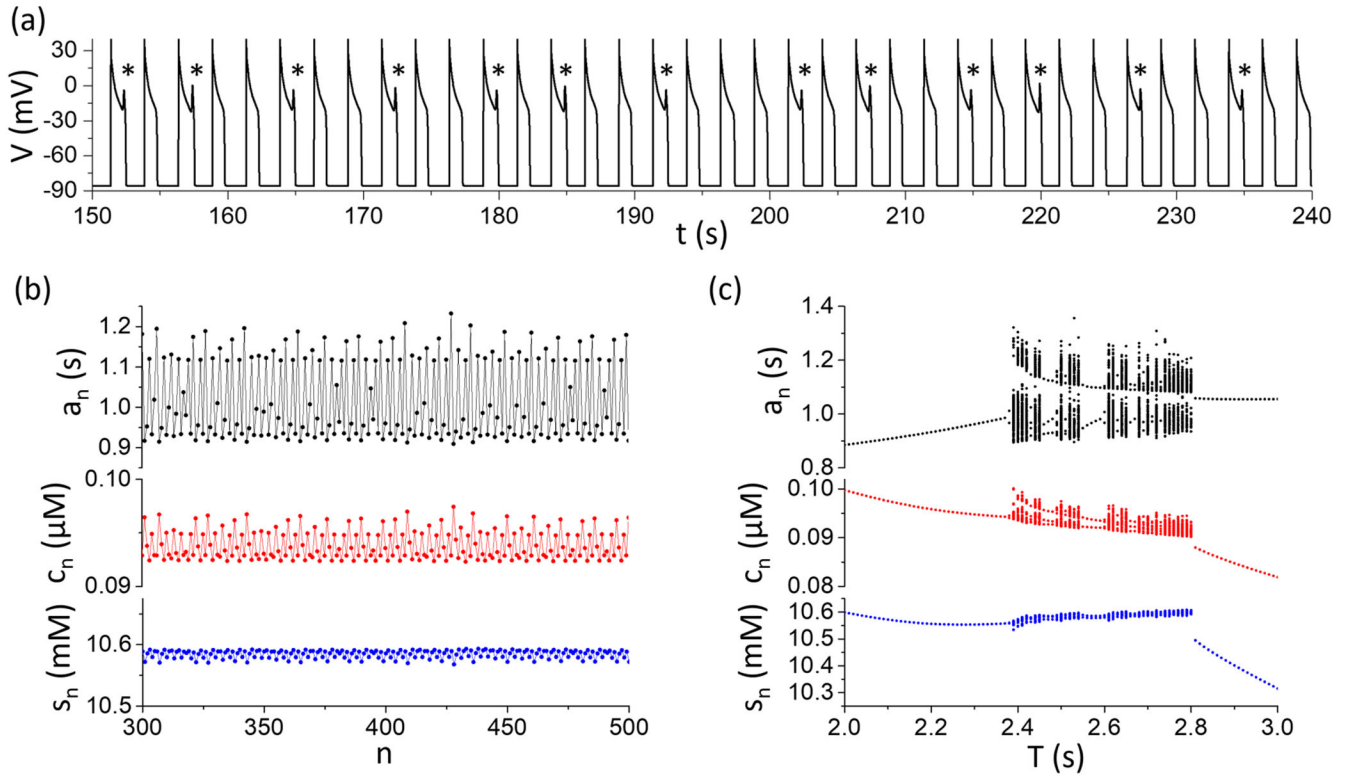
FIG. 12.

Chaotic behaviors in the AP model under the EAD condition. (a) Voltage trace showing chaotic transitions between APs with EADs and APs without EADs. The symbol * marks the APs with EADs. $T = 2.5$ s and $k_{NCX} = 1$ nA/pF. (b) a_n, c_n, and s_n vs n from the same simulation in (a). (c) Bifurcation diagrams showing a_n, c_n, and s_n vs T.

FIG. 13.

Bifurcations and oscillatory dynamics of the IM model for the EAD condition in the oscillatory regime. (a) Replotting the data in Fig. 11(c). All data points are plotted together. Left: a_n vs c_n. Middle: a_n vs s_n. Right: a_n vs z_n after the transform $z_n = s_n - 13000c_n$. (b) a_n, c_n, and s_n vs n from the IM model for $T = 2.5$ s. (c) Bifurcation diagrams showing a_n, c_n, and s_n vs T from the IM model. $g(z_n)$ used in the simulation of the IM model is a piecewise linear function based on the transformed data, plotted as the solid curve in the right panel in (a). The parameters for the functions of $\bar{c}$ and $\bar{s}$ [Eqs. (14) and (15)] are $\gamma_{c0} = 0, \gamma_c = 0.000212, \tau_{ac} = 2.2, \tau_{dc} = 1.5, T_c = 2900, \delta = 8 \times 10^{-6}$, $\Delta = 11, c_0 = 0.0, \gamma_{s0} = 0, \gamma_s = 28.3, \tau_{as} = 1.5, \tau_{ds} = 40, s_0 = 6.8$, and $T_s = 2300$. $\beta_c = 0.2$ and $\beta_s = 0.008$.
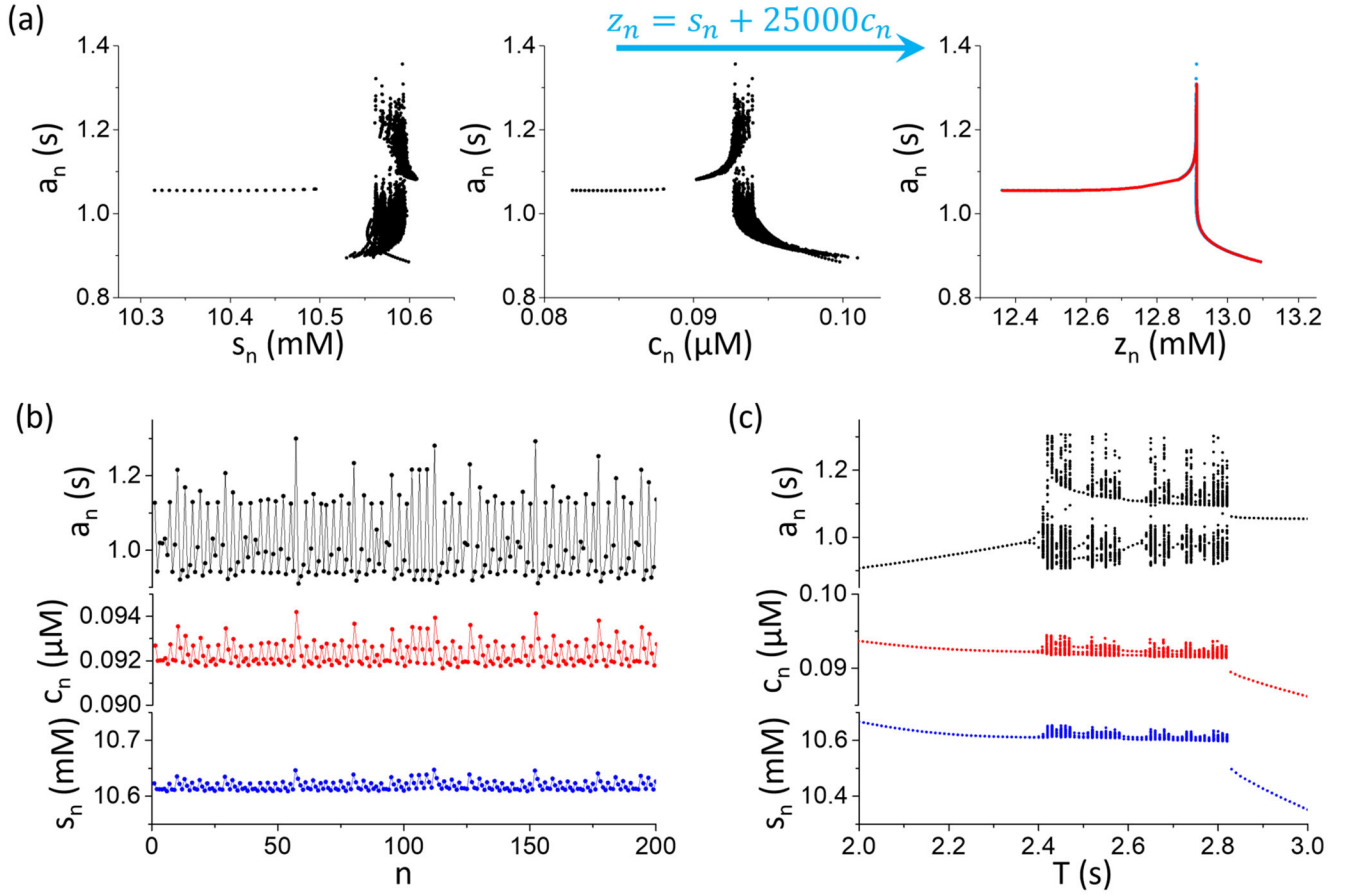
FIG. 14.

Bifurcations and chaotic dynamics of the IM model for the EAD condition under chaotic regime. (a) Replotting the data from Fig. 12(c). All data points are plotted together. Left: a_n vs c_n. Middle: a_n vs s_n. Right: a_n vs z_n after the transform $z_n = s_n + 25000c_n$. (b) a_n, c_n, and s_n vs n from the IM model for $T = 2.52$ s. (c) Bifurcation diagrams showing a_n, c_n, and s_n vs T from the IM model. $g(z_n)$ used in the simulation of the IM model is a piecewise linear function based on the transformed data, plotted as the solid curve in the right panel in (a). The parameters for the functions of $\bar{c}$ and $\bar{s}$ [Eqs. (14) and (15)] are $\gamma_{c0} = 0$, $\gamma_c = 0.000194$, $\tau_{ac} = 2.2$, $\tau_{dc} = 1.5$, $T_c = 1470$, $\delta = 8 \times 10^{-6}$, $\Delta = 5.3$, $c_0 = 0.0$, $\gamma_{s0} = 0$, $\gamma_s = 14.3$, $\tau_{as} = 1.5$, $\tau_{ds} = 40$, $s_0 = 7.1$, and $T_s = 1640$. $\beta_c = 0.16$ and $\beta_s = 0.036$.
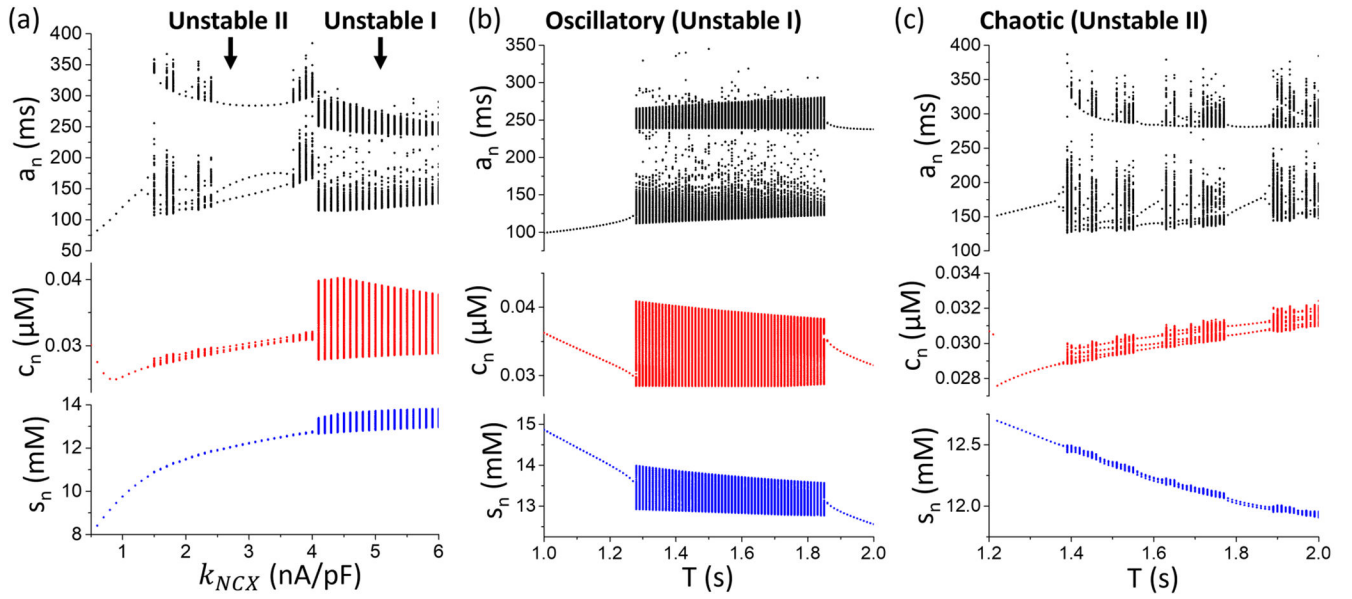
FIG. 15.

Bifurcations and complex dynamics in the AP model under the spike-and-dome condition. (a) Bifurcation diagrams plotting a_n, c_n, and s_n vs k_{NCX} for $T = 1.6$ s. (b) Bifurcation diagrams plotting a_n, c_n, and s_n vs T for the AP model in the unstable I regime ($k_{NCX} = 5$ nA/pF). (c) Bifurcation diagrams plotting a_n, c_n, and s_n vs T for the AP model in the unstable II regime ($k_{NCX} = 3$ nA/pF).
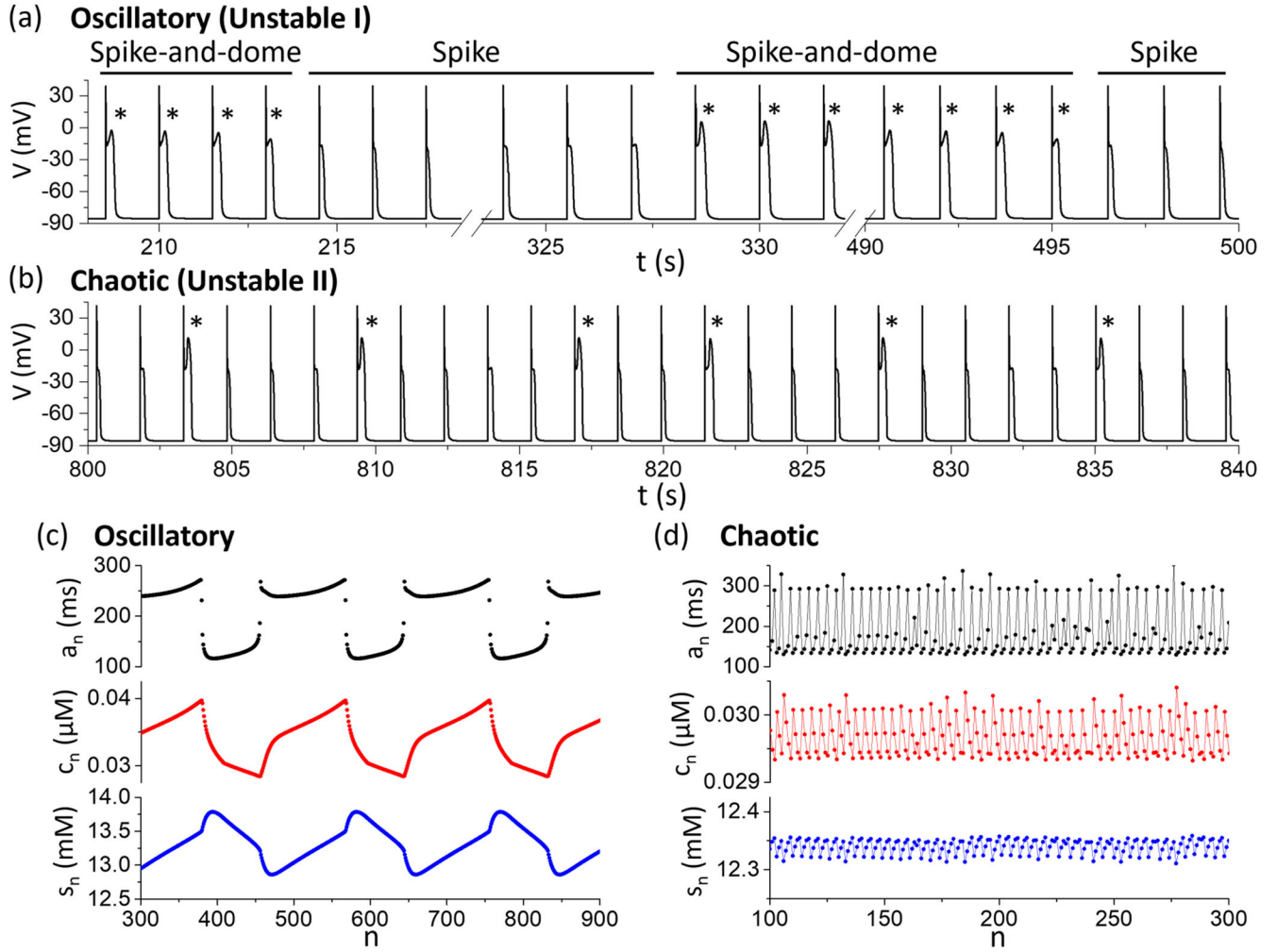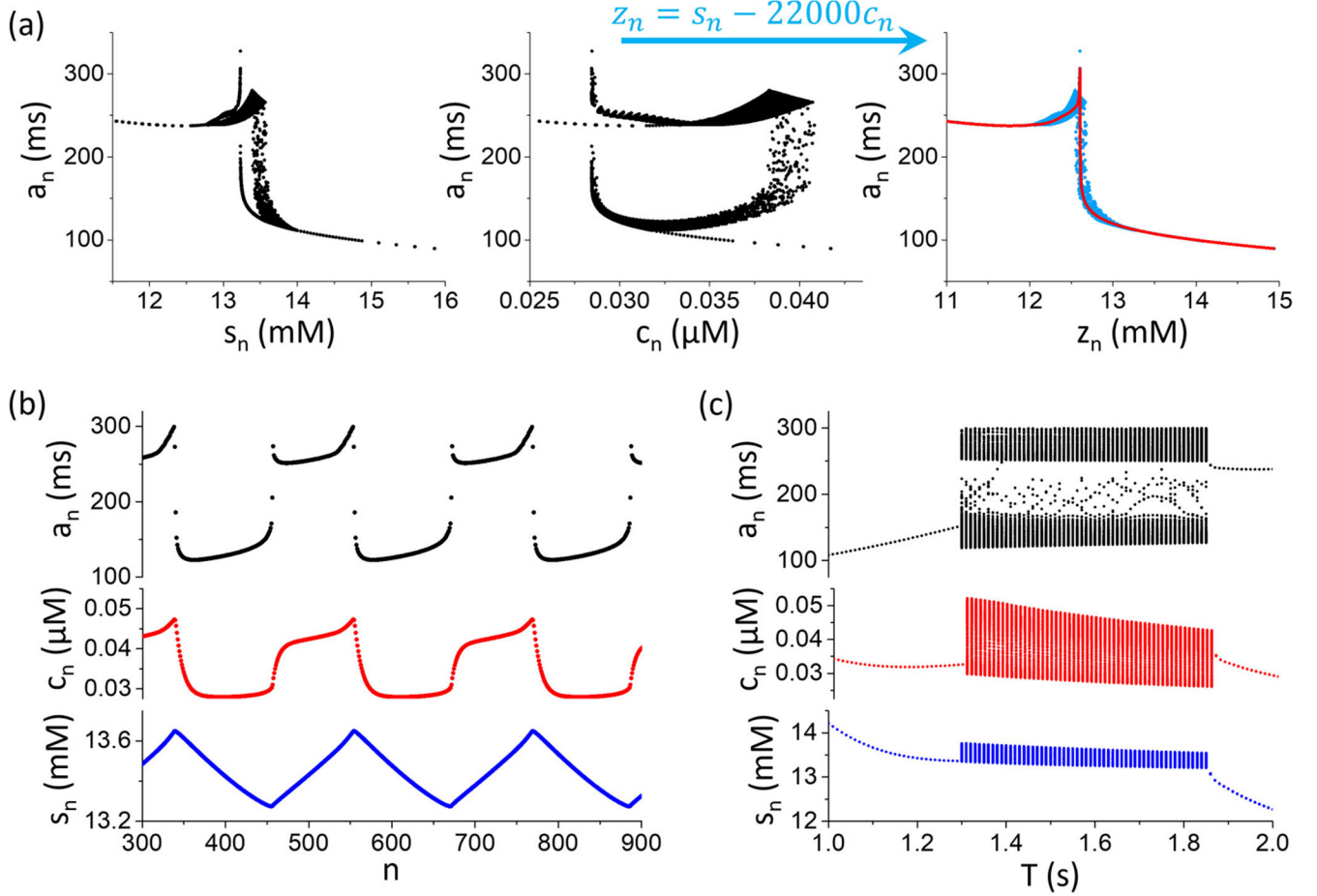
FIG. 16.

Complex dynamics in AP model under the spike-and-dome condition. (a) Voltage vs t for an oscillatory case. $k_{NCX} = 5$ nA/pF and = 1.5 s. (b) Voltage vs t for a chaotic case. $k_{NCX} = 3$ nA/pF and = 1.51 s. (c) a_n, c_n, and s_n vs n for the oscillatory case in (a). (d) a_n, c_n, and s_n vs n for the chaotic case in (b).

FIG. 17.

Recapturing the bifurcations and dynamics using the IM model for the spike-and-dome case in the oscillatory regime. (a) Replotting the data from Fig. 15(b). All data points are plotted together. Left: a_n vs c_n. Middle: a_n vs s_n. Right: a_n vs z_n after the transform $z_n = s_n - 22000 c_n$. (b) a_n, c_n, and s_n vs n from the IM model for $T = 1.5$ s. (c) Bifurcation diagrams showing a_n, c_n, and s_n vs T from the IM model. Oscillatory dynamics occurs between $T = 1300$ ms and $T = 1850$ ms. $g(z_n)$ used in the simulation of the IM model is a piecewise linear function based on the transformed data, plotted as the solid curve in the right panel in (a). The parameters for the functions of $\bar{c}$ and $\bar{s}$ [Eqs. (14) and (15)] are

$\gamma_{c0} = 0, \gamma_c = 0.00015, \tau_{ac} = 100, \tau_{dc} = 70, T_c = -100, \delta = 5.3 \times 10^{-6}, \Delta = 10, c_0 = 0, \gamma_{s0} = 0, \gamma_s = 33,$, $\tau_{as} = 70$

$\tau_{ds} = 60, s_0 = 6.6$, and $T_s = -600$. $\beta_c = 0.126$ and $\beta_s = 0.0013$.
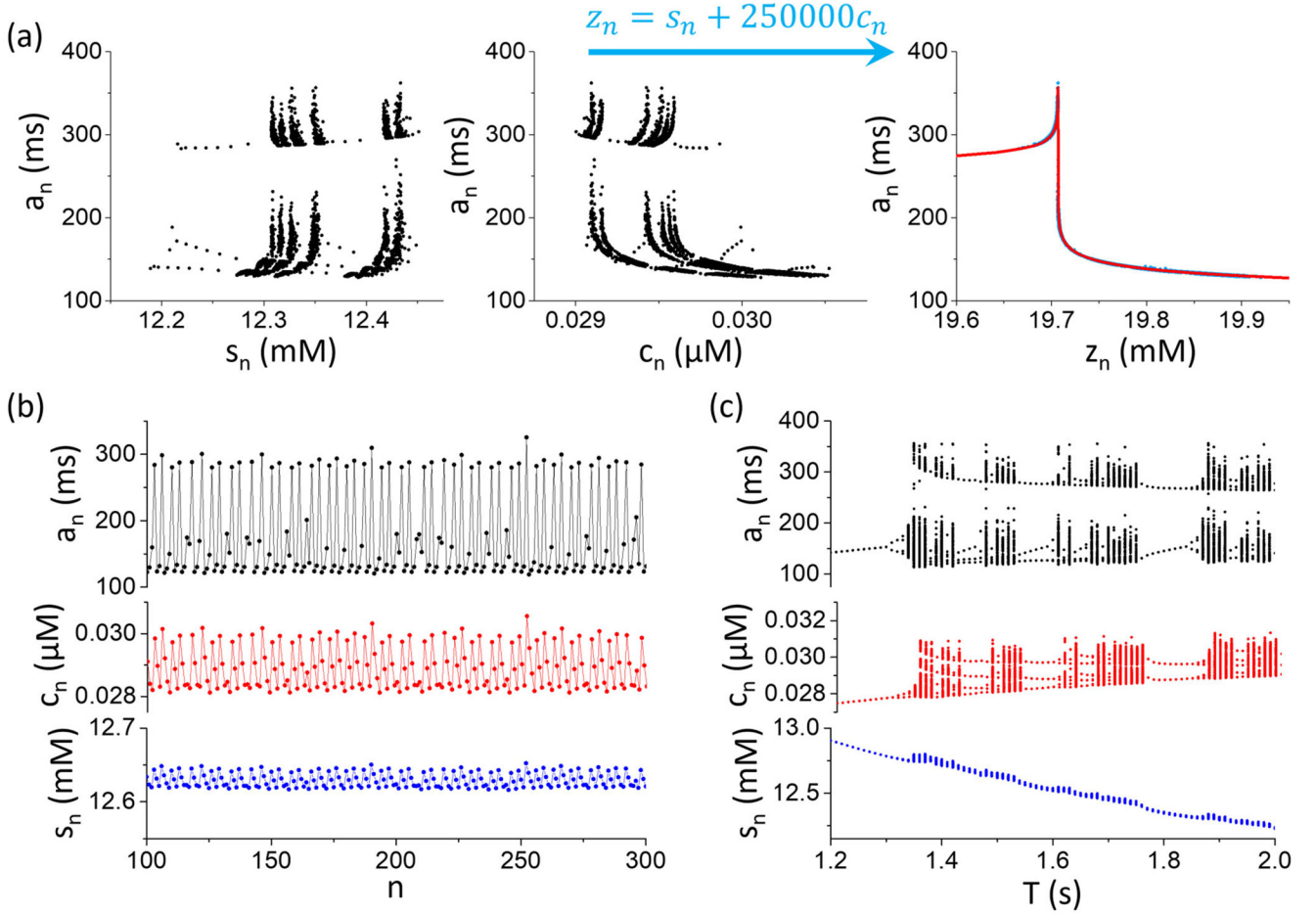
FIG. 18.

Recapturing the bifurcations and dynamics using the IM model for the spike-and-dome case in the chaotic regime. (a) Replotting the data from Fig. 15(c). All data points are plotted together. Left: a_n vs c_n. Middle: a_n vs s_n. Right: a_n vs z_n after the transform $z_n = s_n + 250000c_n$. (b) a_n, c_n, and s_n vs n from the IM model for $T = 1.5$ s. (c) Bifurcation diagrams showing a_n, c_n, and s_n vs T from the IM model. $g(z_n)$ used in the simulation of the IM model is a piecewise linear function based on the transformed data, plotted as the solid curve in the right panel in (a). The parameters for the functions of $\bar{c}$ and $\bar{s}$ [Eqs. (14) and (15)] are $\gamma_{c0} = 0, \gamma_c = 0.00027, \tau_{ac} = 100, \tau_{dc} = 70$, $T_c = 1000, \delta = 4.5 \times 10^{-6}, \Delta = 9.7, c_0 = 0, \gamma_{s0} = 0, \gamma_s = 37, \tau_{as} = 70, \tau_{ds} = 60, s_0 = 7.2$, and $T_s = -400 . \beta_c = 0.12$ and $\beta_s = 0.006$.

TABLE I.

Coupling conditions observed in the AP model and used in the IM model for simulating the bifurcations and complex APD dynamics. "+" in parentheses indicates positive coupling and "−" indicates negative coupling.

AP conditions	Hopf bifurcation (oscillatory)	Period-doubling bifurcation (chaotic)
	Na$^+$-to-APD (−): $g' < 0$ APD-to-Ca^{2+} (+): $u_a > 0$ Ca^{2+}-to-APD (+): $\alpha < 0, \alpha g' > 0$, high NCX	Na$^+$-to-APD (−): $g' < 0$ APD-to-Ca^{2+} (+): $u_a > 0$ Ca^{2+}-to-APD (−): $\alpha > 0, \alpha g' < 0$, low NCX
EAD	APD-to-Na$^+$(+): $w_a > 0$ Fig. 9, Fig. 10, Fig. 11, Fig. 13	APD-to-Na$^+$(+): $w_a > 0$ Fig. 9, Fig. 10, Fig. 12, Fig. 14
Spike and dome	APD-to-Na$^+$(+ / −): $w_a > 0$ or $w_a < 0$ Fig. 15, Fig. 16, Fig. 17	APD-to-Na$^+$(+ / −): $w_a > 0$ or $w_a < 0$ Fig. 15, Fig. 16, Fig. 18